# An Analysis of Modeling Sensitivity Effects for High Lift Predictions using the Flow360 CFD Solver

Thomas Fitzgibbon[*], Philippe Spalart[†], Jim Bungener[‡]
*Flexcompute Inc, Belmont, Massachusetts, 02138*

Qiqi Wang[§]
*Flexcompute Inc, Belmont, Massachusetts, 02138*
*Massachusetts Institute of Technology, Cambridge, Massachusetts 02139*

**This paper presents the contribution of Flexcompute to the 4th High Lift Prediction Workshop based on the Flow360 solver. The analysis of the high-lift prediction results is focused on four key areas: mesh sensitivity, turbulence modelling sensitivity, effect of cold- vs warm-starts and an examination of hysteresis effects. The mesh sensitivity study includes the use of different mesh topologies, families and levels of mesh refinement for the committee and non-committee provided grids. Through the analysis of the resolution of the different flow features recommendations are put forward regarding meshing for future workshops. Next, results are presented using different RANS-based turbulence models, with a focus on the eddy viscosity levels in the flow structures and separated flow predictions. Following, a detailed analysis is performed for comparing cold-starts versus warm-starts with a focus on comparing the differences in the skin friction and flow fields at each angle of attack. Hysteresis effects are also examined to establish the effect of the initial condition on the solution. Finally, the best practice RANS results are analyzed in detail along with DES simulations with the aim to provide conclusions of the ability of RANS to predict high lift flows. The DES results were found to significantly improve the comparison with experimental data and showed high confidence in terms of achieving the correct answer for the right reasons.**

## I. Introduction

High lift predictions are still a major challenge within the CFD community, due to the complexity of flow conditions near $C_{L_{MAX}}$. The complexity is associated with prediction of turbulent separated flows and multiple unsteady flow features including interacting vortices and shear layers. While CFD can be considered as calibrated at cruise conditions [1], further improvements are required for accurate predictions at take-off/landing conditions. Accurate predictions can lead to reduced future programme development costs and risk as well as enable high-lift aerodynamic optimization, which is crucial for the development of new aircraft designs.

To march towards these goals, a series of AIAA High Lift Prediction Workshops has been launched with the current work forming part of the 4th AIAA High Lift Prediction Workshop. The main aims of the series of AIAA High Lift Prediction Workshops is to assess and improve the current CFD modelling capabilities and to provide practical guidelines for accurate CFD predictions [2]. Significant efforts to improve the CFD high-lift predictions have been performed in the past three workshops, with clear developments in the CFD modelling capabilities and reduced scatter between different workshop participants. During the 1st workshop, the Trap Wing was investigated, with a major focus on modelling flap/slat support effects [3]. The 2nd workshop focused on the DLR F11 geometry, with test cases examining the sensitivity of Reynolds number, transition and slat pressure tube bundles [4]. The 3rd workshop investigated the HL-CRM geometry as well as nacelle installation effects for the JAXA JSM model [5]. During the first three editions of the AIAA High Lift Prediction Workshops, the majority of simulations were RANS-based with limited submissions involving scale-resolving simulations, due to high computational costs. The grid sizes used by participants have also grown in each edition of the HLPW with limited use of mesh adaptation.

---

[*]CFD Research Scientist
[†]Head of Fluid Mechanics
[‡]CFD Application Scientist
[§]Associate Professor, Department of Aeronautics and Astronautics, MIT. Co-founder of Flexcompute

The current 4th AIAA Prediction Workshop focuses on the HL-CRM geometry with cases including a flap deflection study and a $C_{L_{MAX}}$ study. A greater emphasis is also put on code verification with a turbulence model verification study for a 2D multi-element airfoil configuration. For the first time, participants are organized into Technology Focus Groups [2]. The workshop examined RANS, hybrid RANS-LES and WMLES modelling approaches as well as investigated high-order discretization and mesh adaptation for RANS. Comparing to the CFD capabilities used in previous workshops, clear development trends are identifiable with a push towards scale-resolving simulations and mesh adapted RANS-based solutions. The current best modelling practices, however, are still a significant unknown for accurate predictions at high-lift, especially for scale-resolving simulations. A greater focus is also put on understanding what flow physics are important to capture within the CFD solutions, with increasing surface and volume flow visualization, including surface skin friction and streamlines as well as off-body vorticity contours. These post-processing aspects also allow for investigations in terms of whether the solutions obtain the correct answer for the correct reasons and whether any cancellation errors exist in the integrated load predictions.

The focus of the current paper is on establishing best practices for high-lift RANS predictions near $C_{L_{MAX}}$ using the Flow360 solver. The key modelling approaches identified for this study, are mesh sensitivity effects, turbulence modelling effects and solution strategies which are examined in the first part of the results section in this paper along with an examination of hysteresis effects based on RANS solutions. The second part of the paper is focused on a greater analysis of the best-practice RANS results, supported by results from scale-resolving DES simulations.

## II. Flow360 Solver

Flow360 is based on hardware/software co-design with emerging hardware computing leading to unprecedented solver speed without sacrifices in accuracy. The Flow360 solver is a node-centered unstructured grid solver based on a 2nd order finite volume method. The convective fluxes are discretised using the Roe Riemann solver, whereas central differences are used for the viscous fluxes. MUSCL extrapolation is used to achieve higher order accuracy in space. Flow360 includes a number of standard turbulence models including SA-neg, SA-RC, $k - \omega$ SST, and DDES. Transition modelling capabilities are also available based on the 3-equation SA-AFT model, but are not used in the present work.

## III. Geometry, Test Conditions and Meshes

The focus of the current work is the HL-CRM geometry [6] shown in Figure 1. This geometry consists of a 10% scale model half-span aircraft in high-lift take-off/landing configuration including many of the detailed geometric components such as the slat brackets, flap track fairings, nacelle chine and junctures between the wing and flaps/slats. Although multiple cases were examined during the HLPW4, the focus of the current paper is on examining the sensitivity effects for the $C_{L_{MAX}}$ study, case 2a. This case involves an alpha sweep ($2.78^o$ to $21.47^o$ for the nominal flap deflection angle of $40^o/37^o$. The freestream Mach number is equal to 0.2 and the freestream Reynolds number based on MAC is equal to 5.49 million. All simulations are performed in free-air without modelling the wind tunnel walls or test stand. The simulations are ran as fully-turbulent without modelling transitional effects. Experimental data is available [7] from measurements in the Qinetiq wind tunnel for the integrated loads (both corrected and uncorrected for wall effects), surface pressures and surface oil-flows. Additionally, unsteady surface pressure measurements are planned in the future. The surface pressure measurement locations are shown in Figure 2. Additionally, for the evaluation of different sensitivity effects, non-dimensional vorticity magnitude was extracted from the CFD solutions along five different planes (even though no experimental data is available), with the plane locations shown in Figure 3.

For the current study, committee-based Pointwise meshes and unstructured meshes from BETA-CAE (labeled as ANSA grids) were used, available on the HLPW4 website [9]. Four different levels of the Pointwise grids were initially used (families 2.1-2.3 on [9]), with a modified version of the D grid (family 5 on [9]) used for the $C_{L_{MAX}}$ study, which added prism layers in the gap between the slat bracket and slat lower surface. Three levels of the ANSA family grids (family 103 on [9]) were also used. A summary of cases with grids used for the current study is shown in Table 1. A cold-started solution is defined as started from free-stream conditions, whereas a warm-started solution is initialised from the previous angle of attack solution in the alpha sweep.

Before presenting the results from the cases seen in Table 1, a preliminary analysis is performed for the ANSA C and PW D level grids, to examine the differences of two grids with similar resolution, but created by two different users. The surface areas at three key regions of the flow field can be seen in Figure 4, whereas volume cuts are shown at 3 of the vorticity measurement slices (Cut 1, Cut 3 and Cut 5, refer to Figure 3) are shown in Figure 5.

The surface and volume grid visualizations show that two different strategies were used when generating the grids.
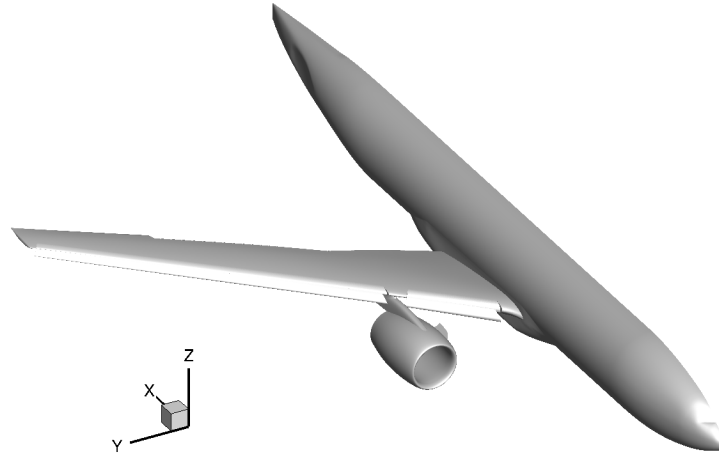
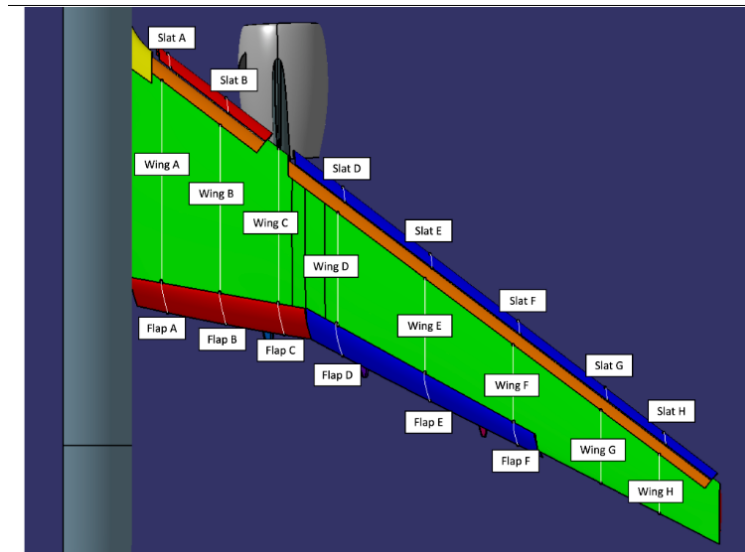**Fig. 1   Geometry of the HL-CRM configuration.**



**Fig. 2   Locations of spanwise cuts with experimental surface pressure data [8].**

The Pointwise mesh, has a finer surface grid with limited target off-body refinement, whereas the ANSA grid uses a coarser surface grid with finer targeted refinement mesh regions in both the surface and volume grids. The ANSA grid targets the flow features coming from the nacelle pylon, chine, outer inboard and inner outboard flaps and flap junctions. The surface refinement is propagated downstream over the wing surface, aimed at preservation of these vortices. The Pointwise grid uses a more uniform surface grid spacing. The Pointwise grid spacing is, however, finer away from the ANSA targeted surface refinement region, on the nacelle surface as well as the root and tip regions of the wing. Similar observations can be made for the volume grids looking at the three extracted cuts. For all cuts, the Pointwise grids have lower cell volumes in the prism layers due to the finer surface grid and lower chordwise spacing. The Pointwise grid does use off-body grid refinement in a more uniform manner, targeting the aircraft wake as a whole
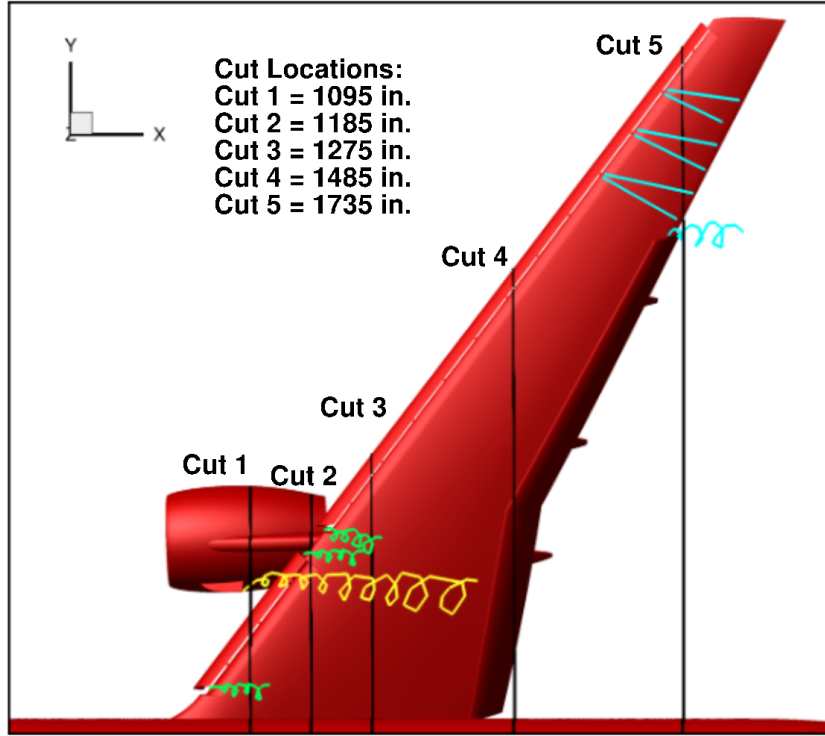
**Fig. 3  Locations of axial cuts for off-body vorticity extraction. Modified based on [8]**

**Table 1    List of cases and meshes used during the current study.**

| Case | Conditions | Meshes | Grid Resolution (nodes) |
|---|---|---|---|
| RANS Mesh Sensitivity - Refinement study | Full $\alpha$ sweep | ANSA A | 68M |
| | | ANSA B | 138M |
| | | ANSA C | 218M |
| RANS Mesh Sensitivity - Topology + Refinement study | $7.05^o$ | PW A Tet | 12M |
| | | PW B Tet | 32M |
| | | PW C Tet | 91M |
| | | PW A Prism-Tet | 12M |
| | | PW B Prism-Tet | 32M |
| | | PW C Prism-Tet | 91M |
| | | PW A Hex-Tet | 12M |
| | | PW B Hex-Tet | 32M |
| | | PW C Hex-Tet | 92M |
| RANS Mesh Sensitivity - Grid Family study | Full $\alpha$ sweep | PW D v3b | 209M |
| | | ANSA C | 218M |
| RANS Turbulence Model Sensitivity (SA, SA-RC) | Full $\alpha$ sweep | ANSA C | 218M |
| RANS Cold-Warm Start Sensitivity | Full $\alpha$ sweep | ANSA C | 218M |
| RANS Hysteresis Effects | Full $\alpha$ sweep | ANSA C | 218M |
| DES simulations (SA-DES) | $19.57^o, 21.47^o$ | ANSA C | 218M |

(a) ANSA, root region  (b) ANSA, nacelle  (c) ANSA, wing tip region
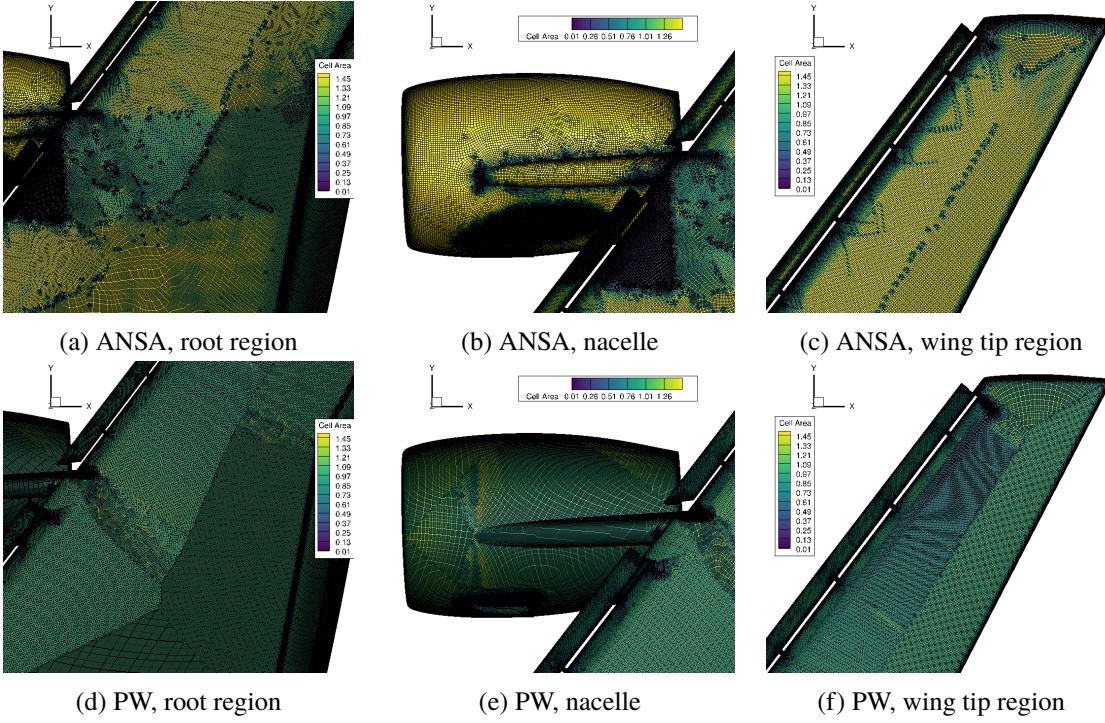
(d) PW, root region  (e) PW, nacelle  (f) PW, wing tip region

**Fig. 4  Surface grid area contours in the root, nacelle and wing tip regions for the ANSA C and Pointwise D level grids.**



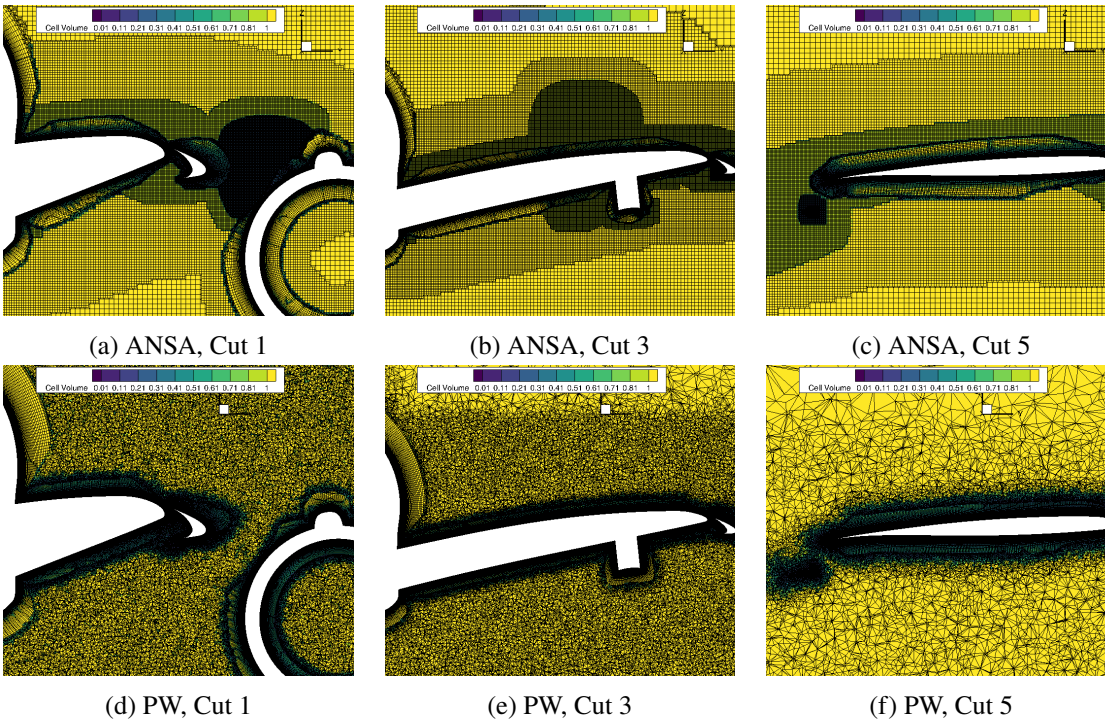(a) ANSA, Cut 1  (b) ANSA, Cut 3  (c) ANSA, Cut 5

(d) PW, Cut 1  (e) PW, Cut 3  (f) PW, Cut 5

**Fig. 5  Surface grid area contours in the root, nacelle and wing tip regions for the ANSA C and Pointwise D level grids.**

rather than individual flow features. The ANSA grid has a very fine grid in the region where the chine vortex passes, as well as target refinement in other regions of the root, inboard of the nacelle, as well as over the wing tip. One of the issues with both grids, which is more prominent for the ANSA grid is the transition between the prism layer grids and off-body regions. This is in particular visible in cut one, where the prism layer grid over the nacelle pylon is much coarser than the surrounding off-body refinement, leading to a discontinuous cell size. Any flow features (nacelle/pylon vortices), going through the coarse grid into the off-body refinement will already be dissipated, limiting the effect of the refinement region. The transition appears to be smoother for the Pointwise grid although a similar band of finer cells is seen in this region. A non-smooth transition can also be seen for the ANSA grid in the wing tip region, with the Pointwise grid showing a smooth transition between the prism layer and off-body grid. During the present work, the ANSA C grid was primarily used, as the Pointwise grid initially did not have prism layers in the region between the slat brackets and lower surface of the slat (causing divergence/convergence issues), with a modified version of the Pointwise grid available at a later date.

One other important aspect of the ANSA Level-C and Pointwise Level-D grids is that certain regions of the grid are above $y^+ < 1$ as seen in Figure 6. The ANSA grid has a $y^+ > 1$ for large regions of the slats, wing and flaps with values close to $y^+ \sim 2$ over the wing and slat leading edge regions where the flow accelerates. The Pointwise grid has a reduced wall spacing compared to the ANSA grid with values of $y^+$ only going slightly above 1 over the slats and wing leading edges. One aspect of the ANSA grid is that it was likely to have been designed for a cell-centered CFD code, whilst Flow360 stores the solution variables at the nodes. This means that for a prism layer grid, the wall distance will typically be double of what it would be for a cell-centered solver. For this reason, primarily the Spalart-Allmaras turbulence model is used, as the Spalart-Allmaras variable is linear at the wall, and hence more forgiving to increased wall y+ than for example the $k - \omega$ SST turbulence model.
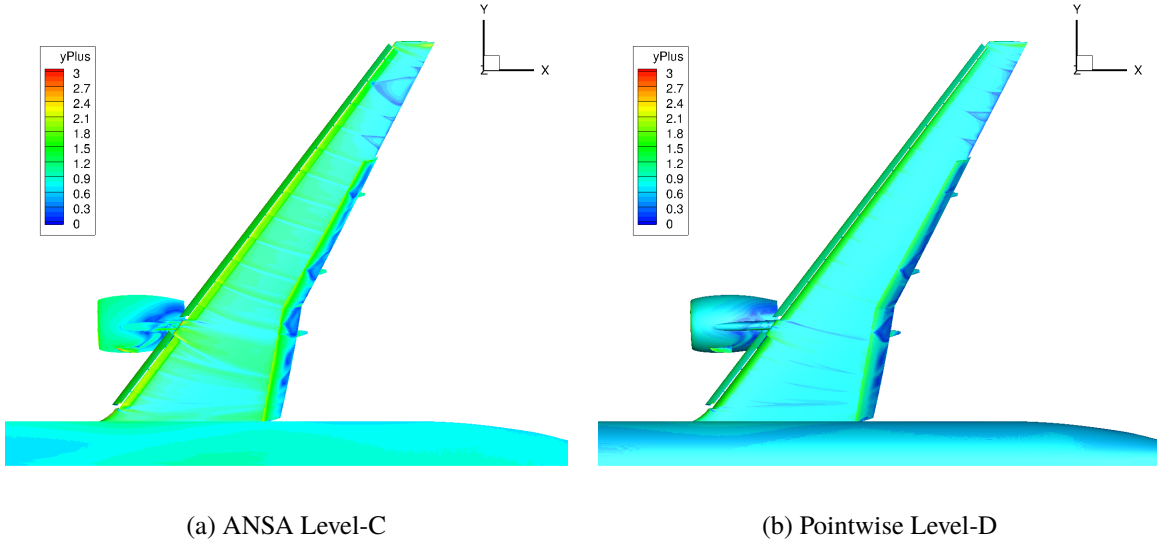


(a) ANSA Level-C             (b) Pointwise Level-D

**Fig. 6 Surface $y^+$ for the ANSA Level-C and Pointwise Level-D grids at $\alpha = 11.29^o$ using warm-started solutions.**

# IV. Results

The results section analyses the high-lift predictions in terms of four key areas: mesh sensitivity effects, turbulence modelling effects, cold-start vs warm-start and hysteresis, which are presented in the following subsections. The last sub-section focuses on comparison of the best-practice RANS results with DES simulations and further experimental data.

## A. Mesh Sensitivity Effects

Firstly, results are presented regarding mesh sensitivity effects. This study includes examination of different mesh topologies (Tet-dominated, Tet-Prism and Hex-dominated), families (Pointwise vs ANSA grids) and levels of mesh

resolution. The effect of mesh resolution is analyzed first by using three different levels of the ANSA family grids. The integrated loads are shown in Figure 7 using cold-started solutions.
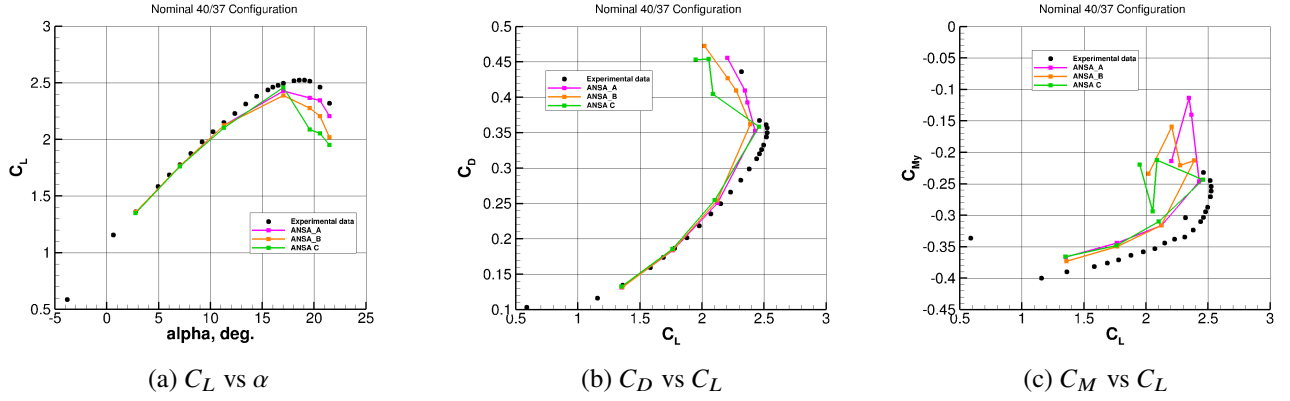


(a) $C_L$ vs $\alpha$      (b) $C_D$ vs $C_L$      (c) $C_M$ vs $C_L$

**Fig. 7** **Integrated loads for different levels of ANSA grid refinement using cold-started solutions.**

The integrated load comparisons show excellent agreement in the linear region with a slight overprediction of the pitching moment, typically seen for RANS solutions. Near $C_{L_{MAX}}$, fairly good agreement is obtained for the ANSA A mesh when compared to experimental data, with mesh refinement leading to poorer predictions at high lift. The finer grids predict sharper stall with lower $C_L$ values at each angle of attack in the non-linear region and higher $C_D$ at a given $C_L$. Mesh levels B and C also predict a earlier high-$\alpha$ pitching moment break compared to experiment. These results are examined further by extracting the surface skin friction distributions at four angles of attack shown in Figure 8.

As can be seen in Figure 8, at $\alpha = 7.05^o$, the three grids show highly similar skin friction contours. A certain amount of separation can be seen on the nacelle and inboard/outboard flaps, with most of the flow being attached over the main wing. The individual vortices, can be identified by a reduction in the local skin friction coefficient, coming from the inboard slat, strake, nacelle pylon and inner outboard slat in the inboard regions of the wing, with the outer slat bracket vortices visible in the outer portion of the wing. As the angle of attack is increased to $\alpha = 11.29^o$, the primary difference between the three grids, is the level of separation seen in the outer portion of the wing. The finer grids lead to higher unphysical separation behind the slat brackets. The biggest differences between the three grids can be observed at $\alpha = 19.57^o$ as the three grids exhibit entirely different flow features in the inboard sections of the wing. The coarsest A level grid, predicts only a minor separation region close to the root of the wing. This separation region is much larger for the finer B level grid, and covers most of the area inboard of the nacelle. For the C level grid, the root region is attached with a large separation region visible past the nacelle over the wing. The three different grids show significant separation over the wing tip and nacelle, which is consistent with grid refinement, indicating that the main effect that changes the integrated loads is the flow topology over the wing in the inboard regions. Similar observations can be made at the angle of attack of $\alpha = 20.55^o$. Here, once again the main difference seen with grid refinement is the level of separation in the root region. Some minor differences are also seen over the nacelle as well as in the level of separation inboard of the blade tip. To examine the effects of grid refinement on the flow field further, vorticity contours are extracted at two angles of attack $11.29^o$ and $19.57^o$ at two locations along the fuselage (Cut 3 and Cut 5, see Figure 3) shown in Figure 9-10, both without and with the grid.

The vorticity fields in the inboard region at $\alpha = 11.29^o$ show that certain features of the flow field are better resolved with grid refinement. In particular this includes, the inboard slat inner and outer vortices as well as the nacelle pylon vortex. The flow structures in the lower surface of the wing are also resolved better, as indicated by higher values of peak vorticity in the vortex cores. However, the key chine vortex which is responsible for energizing the boundary layer and reducing flow separation caused by the nacelle/pylon vortex system [10], is less resolved with increasing grid resolution. One of the potential reasons is that this vortex passes through the regions of the mesh where the coarser prism layer cells meet the refined off-body grid. The stronger vortices outboard of the chine vortex, also have an opposite rotational sense, leading to a weakening of the chine vortex. Similar observations can be made at $\alpha = 19.57^o$, with large regions of separation present in the flow field that affects the location and strength of the individual vortices. For example, for grid C, the chine vortex actually passes inboard of the region which is refined in the mesh, which may have a significant effect on the resultant levels of separation. Further outboard, near the tip region, the flow structures show
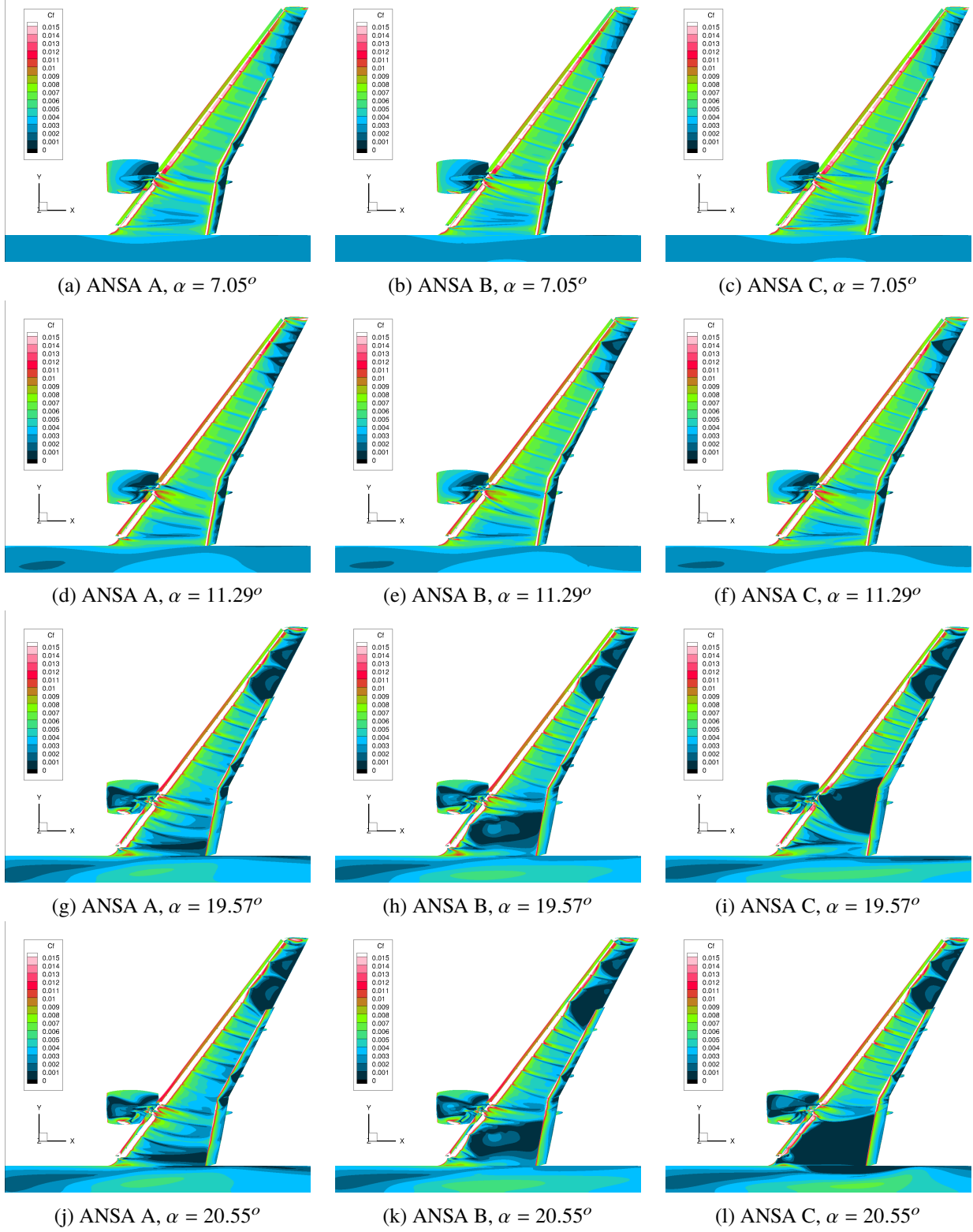
7

(a) ANSA A, $\alpha = 7.05^o$

(b) ANSA B, $\alpha = 7.05^o$

(c) ANSA C, $\alpha = 7.05^o$

(d) ANSA A, $\alpha = 11.29^o$

(e) ANSA B, $\alpha = 11.29^o$

(f) ANSA C, $\alpha = 11.29^o$

(g) ANSA A, $\alpha = 19.57^o$

(h) ANSA B, $\alpha = 19.57^o$

(i) ANSA C, $\alpha = 19.57^o$

(j) ANSA A, $\alpha = 20.55^o$

(k) ANSA B, $\alpha = 20.55^o$

(l) ANSA C, $\alpha = 20.55^o$

**Fig. 8   Skin friction distributions at four angles of attack for different levels of ANSA grid refinement using cold-started solutions.**

(a) ANSA A, $\alpha = 11.29^o$

(b) ANSA B, $\alpha = 11.29^o$

(c) ANSA C, $\alpha = 11.29^o$

(d) ANSA A, $\alpha = 11.29^o$ with grid

(e) ANSA B, $\alpha = 11.29^o$ with grid

(f) ANSA C, $\alpha = 11.29^o$ with grid

(g) ANSA A, $\alpha = 19.57^o$

(h) ANSA B, $\alpha = 19.57^o$

(i) ANSA C, $\alpha = 19.57^o$

(j) ANSA A, $\alpha = 19.57^o$ with grid

(k) ANSA B, $\alpha = 19.57^o$ with grid

(l) ANSA C, $\alpha = 19.57^o$ with grid
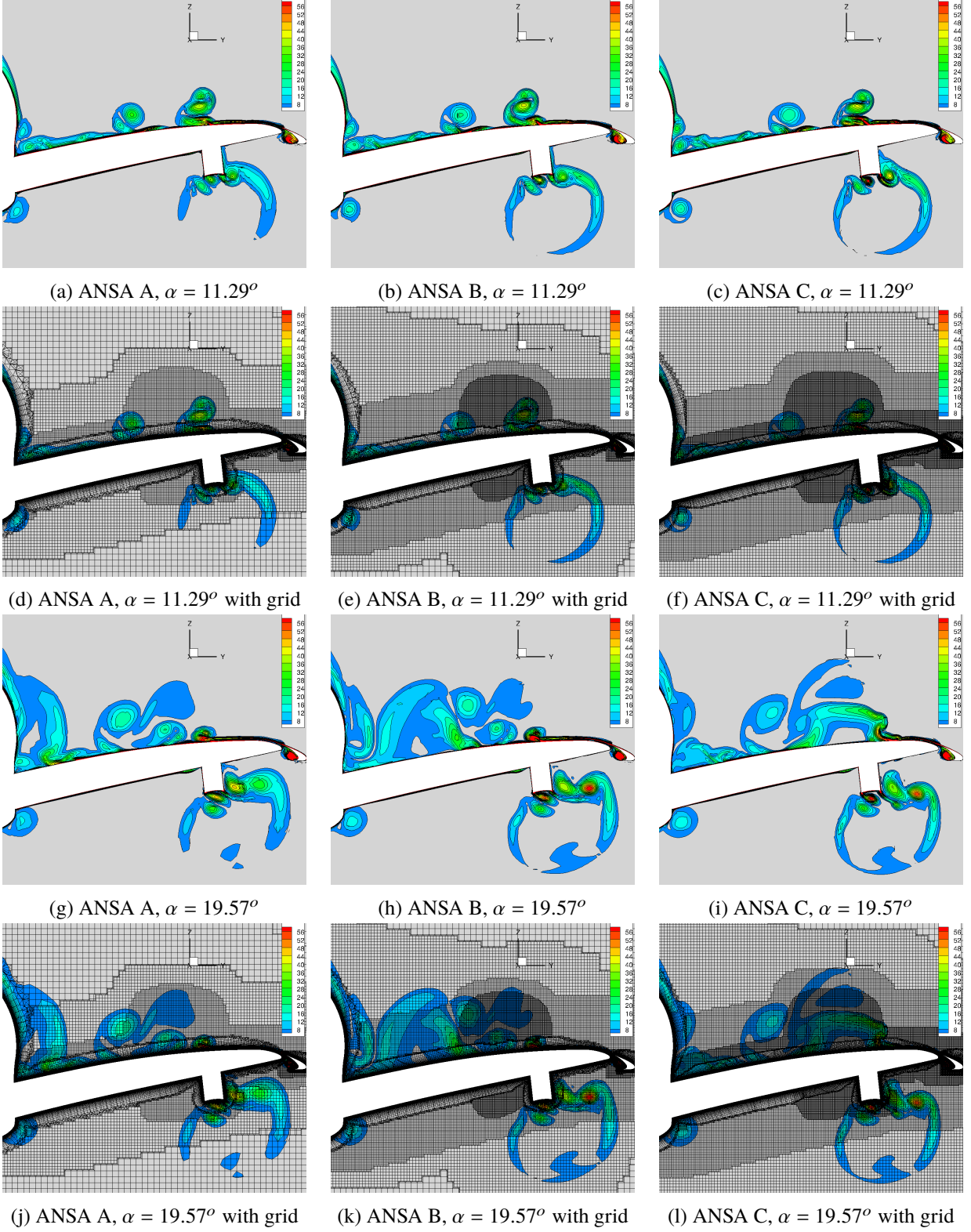
**Fig. 9 Vorticity fields over the wing in the inboard regions (Cut 3) for different levels of ANSA grid refinement using cold-started solutions.**

(a) ANSA A, $\alpha = 11.29^o$

(b) ANSA B, $\alpha = 11.29^o$

(c) ANSA C, $\alpha = 11.29^o$

(d) ANSA A, $\alpha = 11.29^o$ with grid

(e) ANSA B, $\alpha = 11.29^o$ with grid

(f) ANSA C, $\alpha = 11.29^o$ with grid

(g) ANSA A, $\alpha = 19.57^o$

(h) ANSA B, $\alpha = 19.57^o$

(i) ANSA C, $\alpha = 19.57^o$

(j) ANSA A, $\alpha = 19.57^o$ with grid

(k) ANSA B, $\alpha = 19.57^o$ with grid

(l) ANSA C, $\alpha = 19.57^o$ with grid
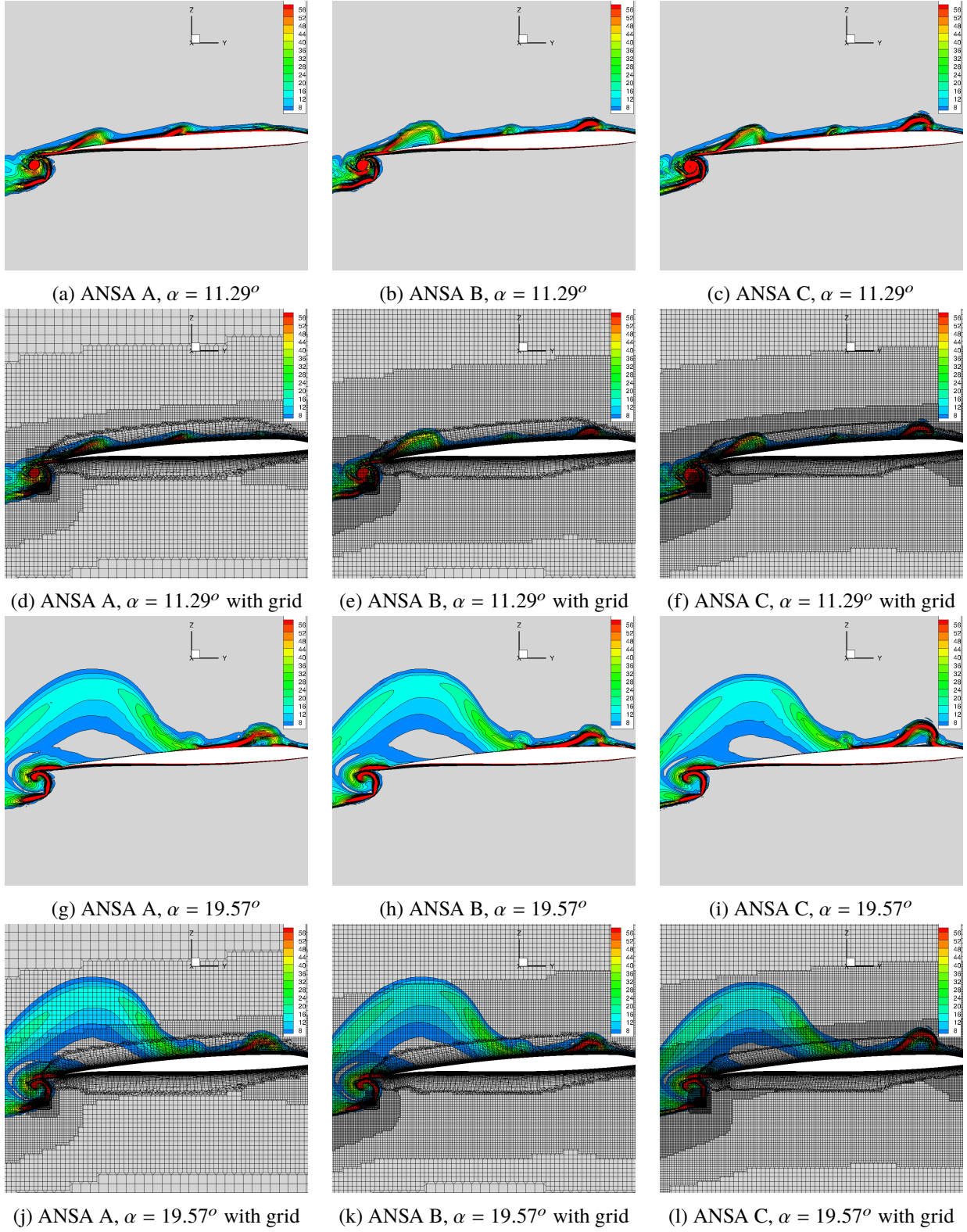
**Fig. 10 Vorticity fields in the outboard regions (Cut 5) for different levels of ANSA grid refinement using cold-started solutions.**

similar features with grid refinement. At $\alpha = 11.29^o$, the slat bracket wakes become resolved better, leading to slightly higher separation across the tip region. The target refinement at the trailing edge also leads to increased resolution of the outboard flap outboard vortex. At $\alpha = 19.57^o$, significant separation can be seen across the tip region, with only minor differences seen with increasing grid refinement and slightly higher separation seen for the wake behind the slat bracket closest to the leading edge of the wing.

Next, the effect of using different grid topologies is examined. For this study, three topologies of the Pointwise grids were used: Tet, Tet-Prism and Tet-Prism-Hex-Pyramid. The study was performed for a single angle of attack of $7.05^o$ using three grid levels: A, B and C (and D for the Hex-dominated grid).The convergence of the integrated loads with grid refinement for the three topologies is shown in Figure 11.



(a) $C_L$          (b) $C_D$          (c) $C_M$
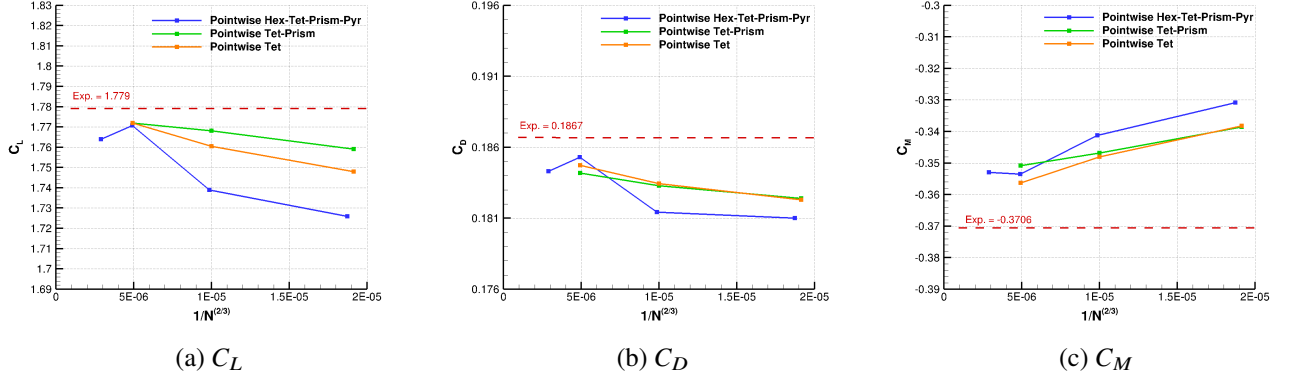
**Fig. 11  Convergence of integrated loads with grid refinement at $\alpha = 7.05^o$ using different Pointwise grid topologies.**

The grid topology study shows that the solutions from the Tet-Prism and Tet grids are consistent for coarser (A, B) grid levels with the Hex-Tet-Prism-Pyramid leading to reduced lift and drag at levels A and B. The lift, drag and moment predictions are in very good agreement across the three topologies for the level C grid. Including the level D grid for the Hex-Tet-Prism-Pyramid grid leads to non-monotonic convergence at this angle of attack, indicating that the solution is still not fully grid independent. The differences in the integrated loads predictions between the level C and D grids, however, are not significant. To examine where the differences between the three grid topologies come from, the skin friction distribution is extracted for the level A and level C grids shown in Figure 12.

Based on the skin friction contours, the largest differences between the three grids can be seen for the Tet-dominated grid, compared to the other two topologies. For both A and C level mesh, a reduced skin friction can be seen in the root region, indicating slightly higher resolution of the inboard vortices. This is despite the fact that the Hex-Tet-Prism-Pyr grid shows the greatest deviation in terms of integrated loads for the Level A grid. The Hex level A grid does, however, show slightly higher separation behind one of the slat brackets in the tip region. The differences between the three grid topologies are not significant especially with grid refinement, as seen in the integrated loads delta values. However, only a single condition of $\alpha = 7.05$ was examined, and hence these observations may not hold should a condition near $C_{L_{MAX}}$ be examined.

Next a comparison of the ANSA C level and Pointwise D level grids is performed. These grids have a similar resolution of around 200 million nodes, but were generated by two different users and meshing software. A preliminary comparison of the differences between the ANSA and Pointwise grids was presented in the previous section of the paper. A comparison of the integrated loads is shown in Figure 13. Here, warm-started solutions are used, where each consequent $\alpha$ is restarted from the previous one, rather than from freestream.

The comparison indicates, similar results in the linear region of the lift curve. As the $\alpha$ is spooled-up further (in between $\alpha = 11.29^o$ and $\alpha = 17.05^o$ the Pointwise grid leads to a slightly higher lift and lower drag at a given lift coefficient. The gradient of the moment curve is also reduced in the linear region for the Pointwise grid. In the non-linear region, the Pointwise grid exhibits a much sharper stall, indicated by a sharp drop in lift coefficient with a poor prediction of the high $\alpha$ pitching moment break. The ANSA grid, predicts a shallow stall, with only a minor underprediction in $C_L$ compared to experimental data. The moment break is also predicted much better for the ANSA grid when compared to the Pointwise grid. Both grids lead to similar results at the highest examined $\alpha = 21.47^o$ with
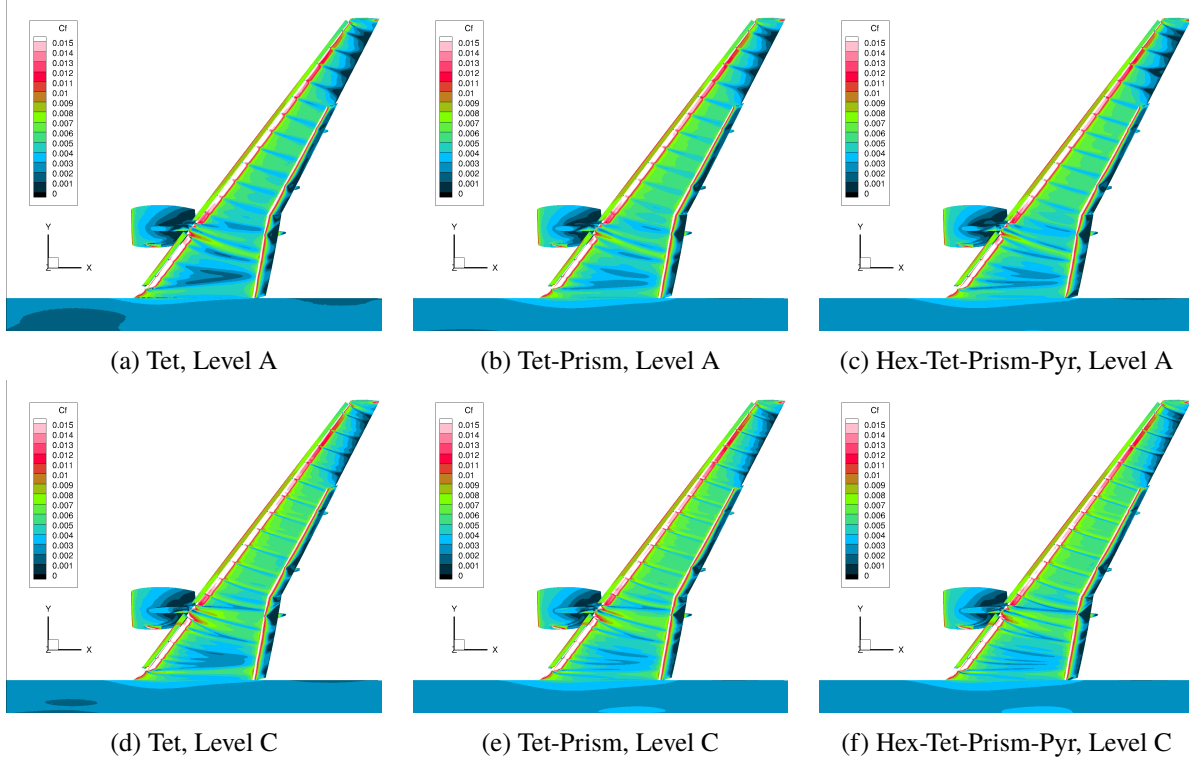
(a) Tet, Level A     (b) Tet-Prism, Level A     (c) Hex-Tet-Prism-Pyr, Level A

(d) Tet, Level C     (e) Tet-Prism, Level C     (f) Hex-Tet-Prism-Pyr, Level C

**Fig. 12  Skin friction distributions at $\alpha = 7.05^o$ for two grid refinement levels of the three different Pointwise grid topologies.**
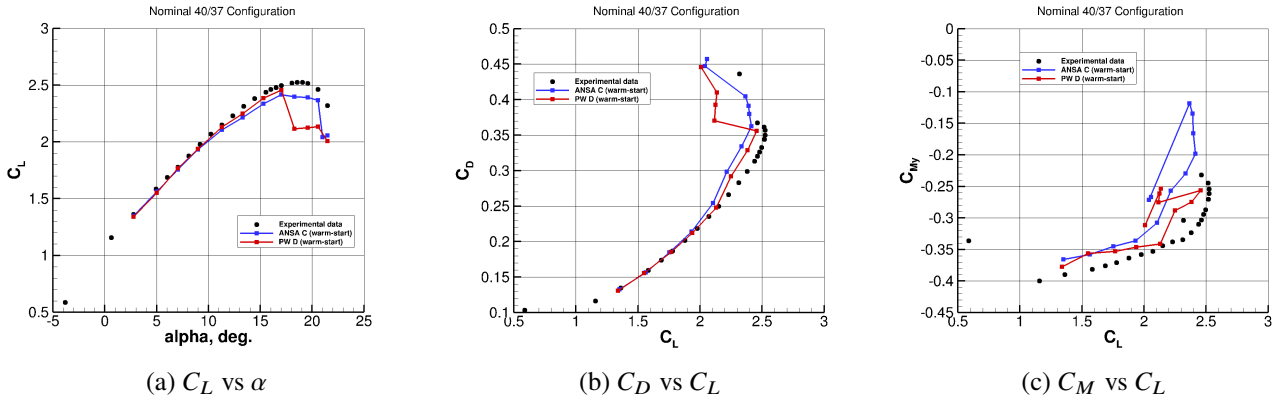


(a) $C_L$ vs $\alpha$     (b) $C_D$ vs $C_L$     (c) $C_M$ vs $C_L$

**Fig. 13  Comparison of integrated loads for ANSA C and Pointwise D level grids using warm-started solutions.**

a underpredicted lift and overpredicted drag when compared to experimental data. The results are analyzed in more detailed by examining the skin friction distributions for both grids focusing on the non-linear region, shown in Figure 14.

The skin friction distributions at $\alpha = 17.05^o$, show that the main reason behind the higher lift coefficient for the Pointwise grid, which is the reduced separation seen in the blade tip region. These changes are due to different behavior of the slat bracket wakes for both grids. For the ANSA grid, strong levels of separation are seen behind two slat brackets with the slat bracket wake in between them exhibiting attached flow. For the Pointwise grid, two slat bracket wakes that are next to each other show high levels of separation, which leads to attached flow for the bracket inboard as well as attached flow for the most outboard slat bracket. The root region shows similar features for both grids, with no significant separation patterns, with low regions of skin friction traced by the individual vortices seen in a typical high-lift system. As the angle of attack is increased to $\alpha = 19.57^o$, the skin friction patterns in the tip region remain

12

(a) ANSA C, $\alpha = 17.05^o$      (b) PW D, $\alpha = 17.05^o$

(c) ANSA C, $\alpha = 19.57^o$      (d) PW D, $\alpha = 19.57^o$

(e) ANSA C, $\alpha = 20.55^o$      (f) PW D, $\alpha = 20.55^o$

(g) ANSA C, $\alpha = 21.47^o$      (h) PW D, $\alpha = 21.47^o$
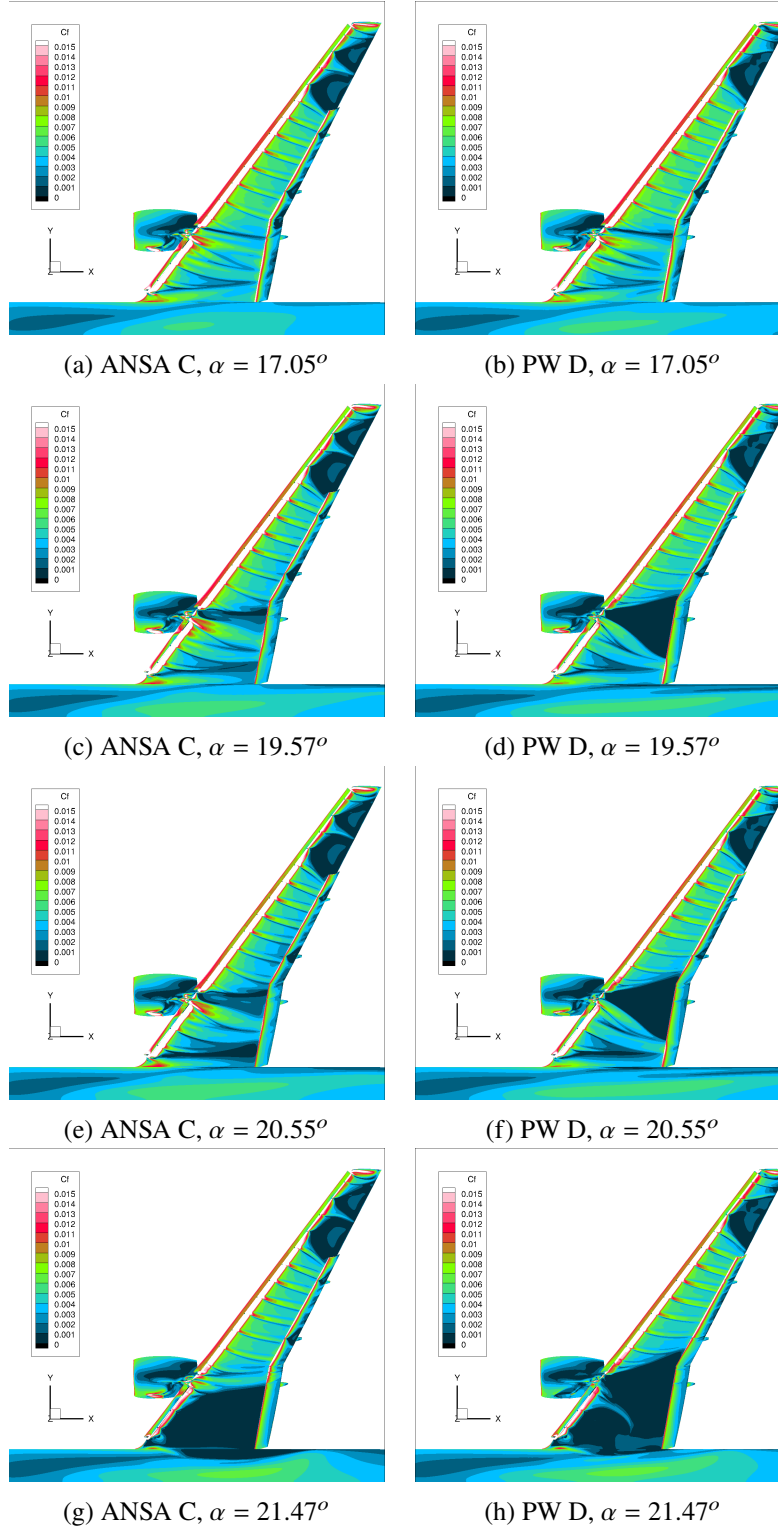
**Fig. 14   Skin friction distributions at four angles of attack for the ANSA C-level and Pointwise D-level grids using warm-started solutions.**

similar as in the previous angle of attack. Significant differences between the two grids are observed over the wing in the

nacelle region, where the flow separates strongly past the nacelle for the Pointwise grid, with only a minor reduction in skin friction seen for the ANSA grid. Both grids show similar skin friction distributions at the root of the wing, where the inner inboard flap and inner flap junction vortex pair passes. The large separation past the nacelle is the main reason for the sharp drop in lift coefficient for the Pointwise grid simulations, which is not present in the ANSA grid results. At $\alpha = 20.55^o$, similar flow patterns are observed both across the blade tip and inboards. The flow begins to separate at the root of the wing, with a slightly wider region of reduced skin friction seen for the ANSA grid. At the highest angle of attack of $21.47^o$, the root is completely separated for both ANSA and Pointwise grids. For the Pointwise grid, the region over the wing past the nacelle remains separated, leading to a very large region of separated flow inboard. The results are examined further by comparing the vorticity contours at five radial stations, and two angles of attack of $17.05^o$ and $19.57^o$, shown in Figures 15-19. The locations of each of the axial stations were presented in Figure 3.



(a) ANSA C, $\alpha = 17.05^o$   (b) ANSA C, $\alpha = 17.05^o$+g   (c) PW D, $\alpha = 17.05^o$   (d) PW D, $\alpha = 17.05^o$+g

(e) ANSA C, $\alpha = 19,57^o$   (f) ANSA C, $\alpha = 19.57^o$+g   (g) PW D, $\alpha = 19.57^o$   (h) PW D, $\alpha = 19.57^o$+g
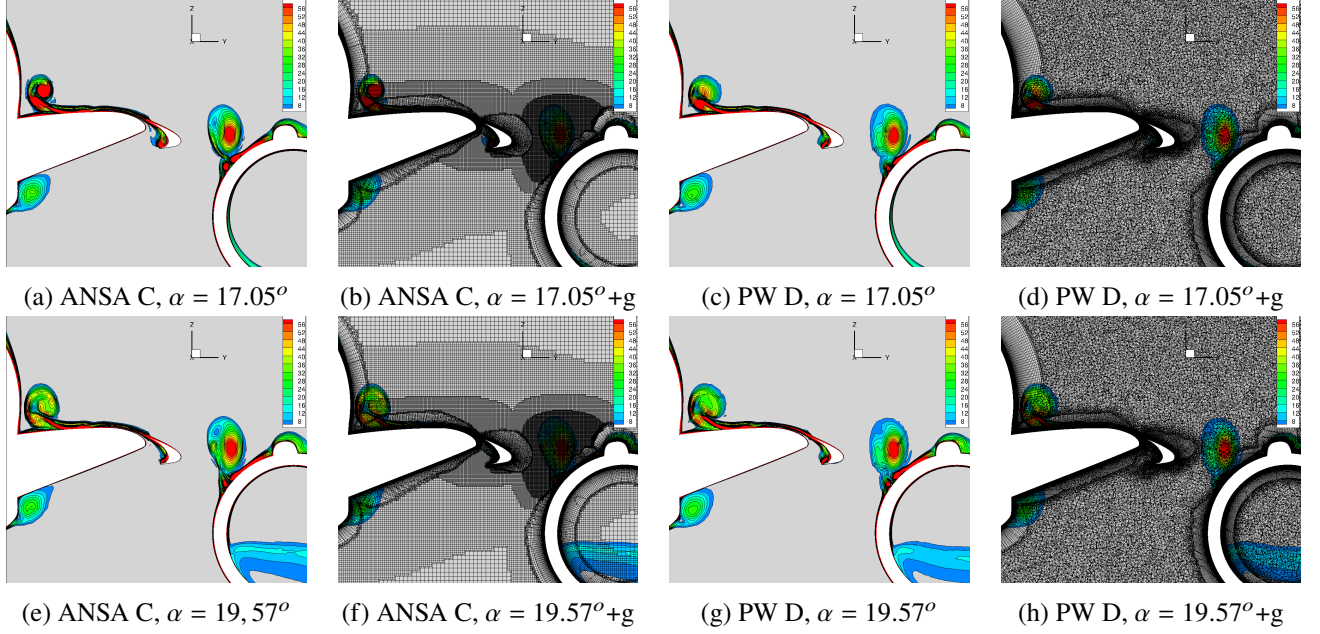
**Fig. 15   Vorticity fields at Cut 1 for the ANSA C-level and Pointwise D-level grids using warm-started solutions, g=grid.**

The vorticity contours indicate that a significant influence of the grid exists based on the flow field features. At Cut 1, the primary flow features seen in the contours are the chine vortex and the inner inboard flap/ inner inboard flap junction vortex pair. At $\alpha = 17.05^o$, the resolution of the chine vortex is similar for both grids, despite the much finer grid used in this region for the ANSA grid with a targeted refinement. The inboard slat vortex pair, however, is much better resolved for the ANSA grid, with higher values of vorticity seen in the vortex cores. At the higher angle of attack of $19.57^o$, the resolution of the vortical structures is comparable for both grids. Further downstream at Cut 2, greater differences are seen. Firstly, the chine vortex shows a higher peak vorticity for the Pointwise grid. The slat shear layer, which rolls up under the chine vortex is also better resolved on the Pointwise grid, especially seen at $\alpha = 17.05^o$. Similar resolution is found for the inner inboard slat vortex pair at $\alpha = 17.05^o$, with slightly higher values of vorticity seen at $\alpha = 19.57$. The outer inboard slat vortex pair is better resolved for the ANSA grid, which may be the main reason of the lower vorticity in the chine vortex core, compared to the Pointwise grid. Another potential reason is the finer surface grid of the Pointwise grid, leading to more grid points in the chordwise direction. The outer inboard slat vortex is of opposite rotational sense, weakening the chine vortex. At Cut 3 similar observations can be made, however, separation is observed over the wing for the Pointwise grid at $\alpha = 19.57^o$, not seen for the ANSA grid. At $\alpha = 17.05^o$, the Pointwise grid shows a stronger chine vortex with a weaker outer inboard slat vortex pair, with a similar resolution of the slat shear layer and the nacelle/pylon twin vortices. As the angle of attack increases to $\alpha = 19.57^o$, the vortex pairs from the nacelle pylon and outer inboard slat interact with each other as well as the slat shear layer. The separation is likely to be caused by poorer resolution of the outer inboard slat vortex pair. The vortical structures below the wing, on the nacelle surface and in the wake of the nacelle are also generally better resolved for the ANSA grid. At Cut 4, the primary differences between the two grids occur at $\alpha = 19.57^o$, where the Pointwise grid shows a large vortical
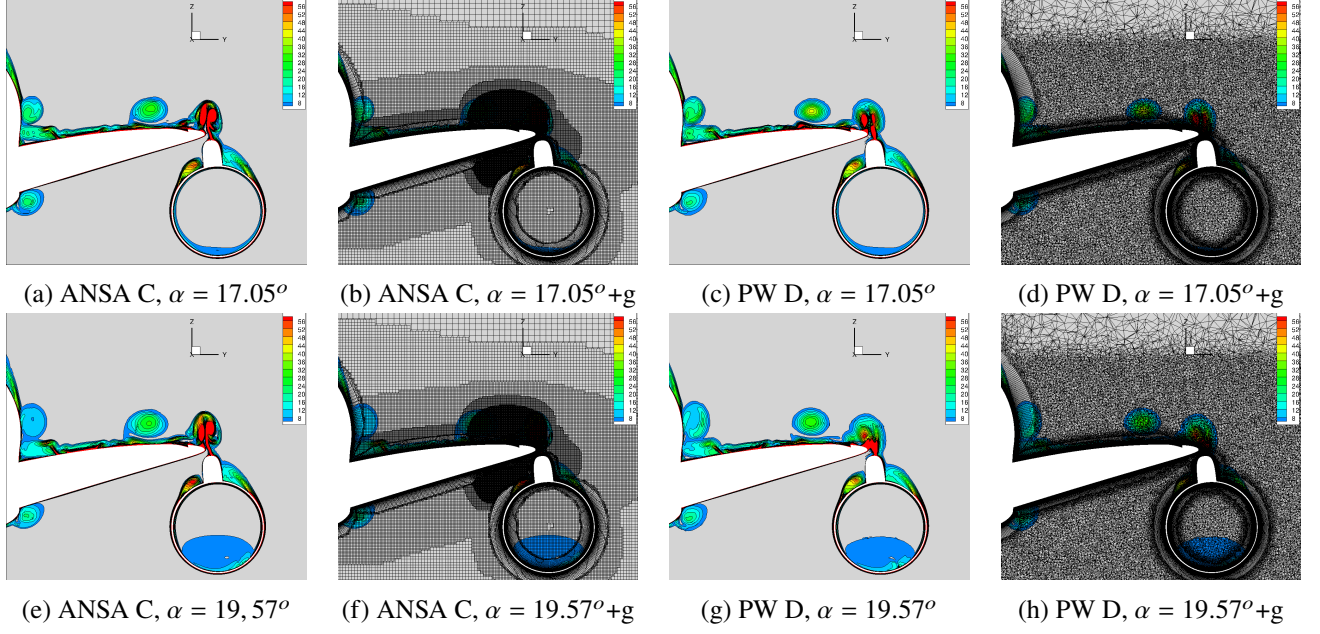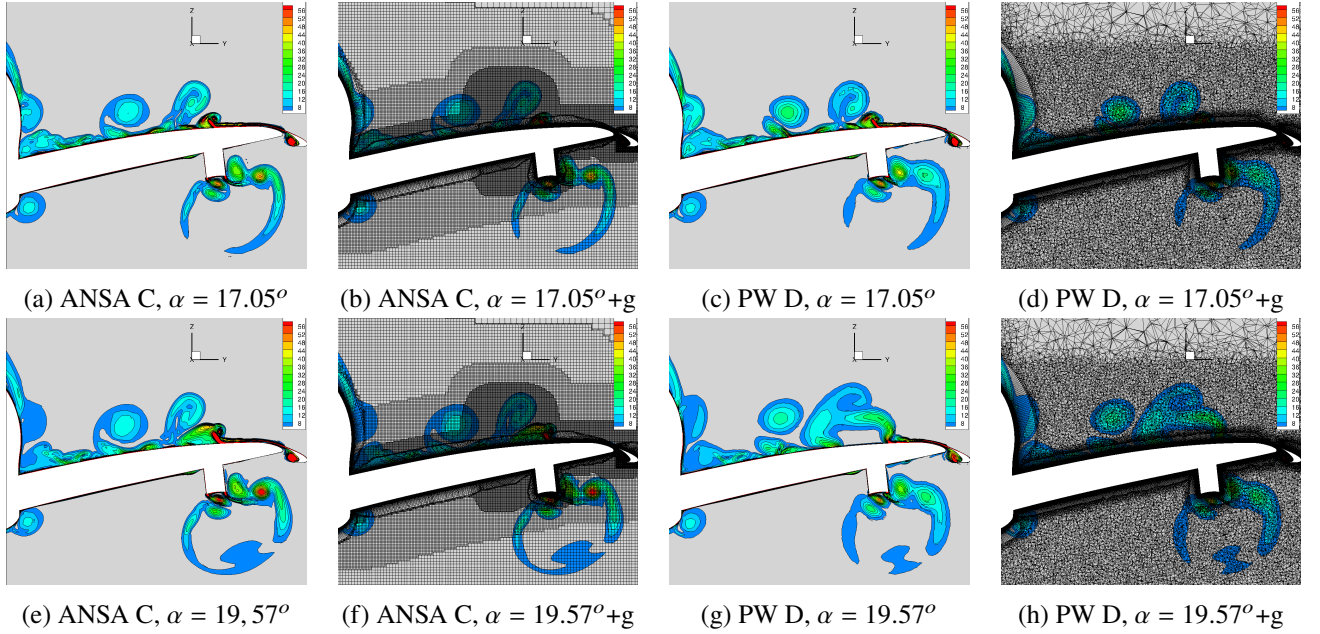
14

(a) ANSA C, $\alpha = 17.05^o$      (b) ANSA C, $\alpha = 17.05^o$+g      (c) PW D, $\alpha = 17.05^o$      (d) PW D, $\alpha = 17.05^o$+g

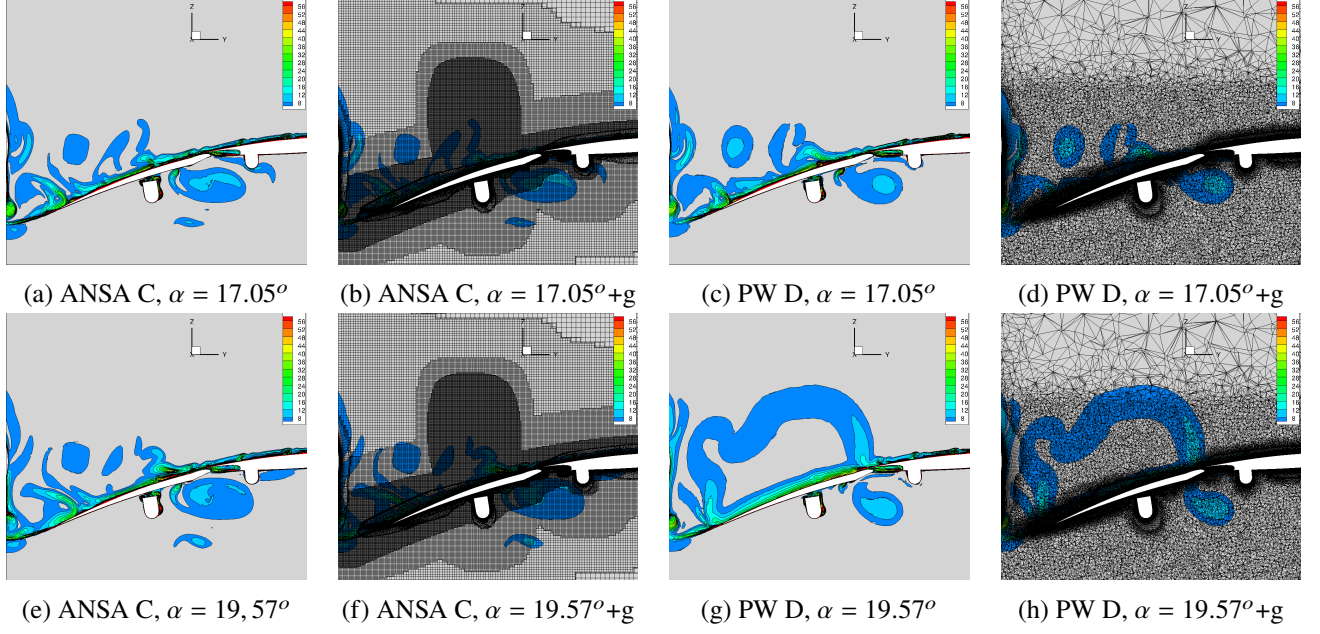(e) ANSA C, $\alpha = 19, 57^o$      (f) ANSA C, $\alpha = 19.57^o$+g      (g) PW D, $\alpha = 19.57^o$      (h) PW D, $\alpha = 19.57^o$+g

**Fig. 16  Vorticity fields at Cut 2 for the ANSA C-level and Pointwise D-level grids using warm-started solutions, g=grid**
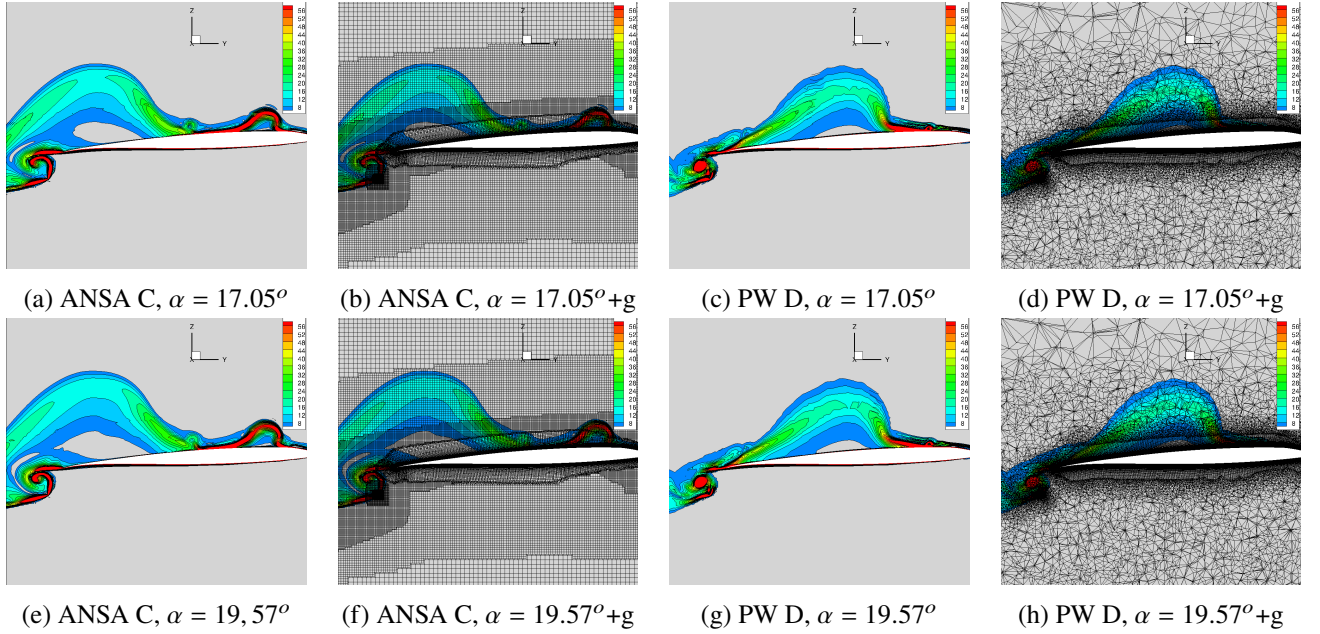


(a) ANSA C, $\alpha = 17.05^o$      (b) ANSA C, $\alpha = 17.05^o$+g      (c) PW D, $\alpha = 17.05^o$      (d) PW D, $\alpha = 17.05^o$+g

(e) ANSA C, $\alpha = 19, 57^o$      (f) ANSA C, $\alpha = 19.57^o$+g      (g) PW D, $\alpha = 19.57^o$      (h) PW D, $\alpha = 19.57^o$+g

**Fig. 17  Vorticity fields at Cut 3 for the ANSA C-level and Pointwise D-level grids using warm-started solutions, g=grid**

structure above the flap coming from the separated wing. The ANSA grid refinement region does not capture any particular vortical features at this station, showing that the grid points could be used elsewhere. At Cut 5 both grids show unphysical separation over the wing in the slat bracket wakes. The separation is slightly weaker for the Pointwise grid, which has a finer grid in the prism layers, but coarser off-body grid. Another significant difference is the much higher resolution of the outer outboard flap vortex for the Pointwise grid.

Based on the mesh sensitivity study it can be claimed that even at 200 million nodes, the high lift predictions are not

(a) ANSA C, $\alpha = 17.05^o$     (b) ANSA C, $\alpha = 17.05^o$+g     (c) PW D, $\alpha = 17.05^o$     (d) PW D, $\alpha = 17.05^o$+g

(e) ANSA C, $\alpha = 19,57^o$     (f) ANSA C, $\alpha = 19.57^o$+g     (g) PW D, $\alpha = 19.57^o$     (h) PW D, $\alpha = 19.57^o$+g

**Fig. 18    Vorticity fields at Cut 4 for the ANSA C-level and Pointwise D-level grids using warm-started solutions, g=grid**



(a) ANSA C, $\alpha = 17.05^o$     (b) ANSA C, $\alpha = 17.05^o$+g     (c) PW D, $\alpha = 17.05^o$     (d) PW D, $\alpha = 17.05^o$+g

(e) ANSA C, $\alpha = 19,57^o$     (f) ANSA C, $\alpha = 19.57^o$+g     (g) PW D, $\alpha = 19.57^o$     (h) PW D, $\alpha = 19.57^o$+g

**Fig. 19    Vorticity fields at Cut 5 for the ANSA C-level and Pointwise D-level grids using warm-started solutions, g=grid**

fully mesh converged. This was particularly seen for the comparison of the ANSA and Pointwise grids, where meshes with similar resolution were generated but with a significantly different approach. In particular, the Pointwise grid used more uniform off-body grid refinements, which were not targeted at resolving particular flow features. Further improvements to the mesh distributions could lead to improved results. The grid topology study shows a low degree of sensitivity for the integrated loads and flow features, although it was only performed for a single angle of attack of $7.05^o$, which is in the linear region of the lift curve. Finally, increasing the mesh resolution does not necessarily lead to

16

improved results for high-lift predictions. In the case of the ANSA grids, increasing the grid resolution led to increased separation both in the inboard and outboard regions of the wing. Another study conducted by NASA [11], also showed increased separation in outer region of the wing with increasing mesh resolution. The behavior of the flow topology in the inboard regions, can be attributed to a high mesh sensitivity and the need to resolve many vortical structures present in the flowfield. Whereas, the flow topology predictions in the outer wing due to the slat bracket wakes, with unphysical separation present in many RANS-based solutions are likely to be a feature of RANS-based solutions, which are not likely to improve with increased grid refinement. Based on the results presented in the mesh sensitivity study, it is recommended to perform coarse grid simulations to locate the key flow structures, and place targeted refinement regions based on the coarse grid results. Another recommendation is to ensure that the transition between the prism layer and off-body grid is as smooth as possible.

### B. Turbulence Modelling Effects

The focus of the current section is the comparison between Spalart-Allmaras turbulence model with and without the rotation correction. Typically, the addition of the rotation correction leads to a reduction in eddy viscosity levels in the vortical structures. This can both lead to stronger flow features in terms of vorticity, but also reduced overall solution damping. The main aim of this section is to determine what effect the rotation correction has on the prediction of flow separated regions inboard as well as over the wing tip. For this study, the ANSA C grid was used with warm-started solutions. Firstly, the integrated load predictions are compared, shown in Figure 20.



(a) $C_L$ vs $\alpha$      (b) $C_D$ vs $C_L$      (c) $C_M$ vs $C_L$
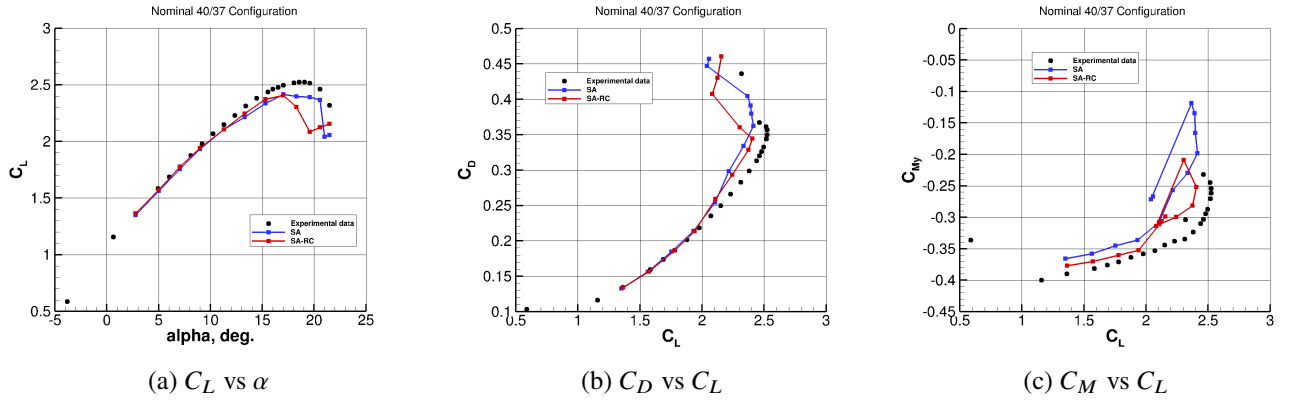
**Fig. 20    Comparison of integrated loads for cases with the SA and SA-RC turbulence models using warm-started solutions.**

The integrated loads show similar predictions for SA and SA-RC turbulence models in the linear region in terms of lift and drag. The main difference between the two models is the pitching moment prediction which is closer to experiment for the SA-RC model. The SA-RC model, however, predicts a different behavior for the low-alpha pitching moment break, with a sharp change at $\alpha = 11.29^o$ and much lower gradient before $\alpha = 17.05^o$. In the region of $\alpha = 11.29 - 15^o$, the SA-RC model also predicts a slightly higher lift coefficient and lower drag. At $\alpha = 17.05^o$, both models show similar predictions with only minor differences in the drag and moment predictions. The greatest difference between the two turbulence models occurs near $C_{L_{MAX}}$, as the SA-RC model predicts stall at an earlier $\alpha$, but recovers to an increased lift at the highest angle of attack of $\alpha = 21.47^o$. The SA model drag and moment predictions are much closer to experiment with the SA-RC model leading to overpredicted drag and poor prediction of the high-alpha pitching moment break. The differences in the integrated loads are examined in more detail by comparing the skin-friction distributions for the SA and SA-RC turbulence models at four angles of attack, shown in Figure 21.

Based on the skin friction distributions, at $\alpha = 11.29^o$, the tip region shows different features for SA and SA-RC simulations, as strong unphysical separation is seen behind different slat brackets. The root region flow patterns at $\alpha = 11.29^o$ show similarities, with slightly different separation patterns seen on the inboard flap. At $\alpha = 17.05^o$, the separation regions in the tip region grow significantly. There are two distinct regions of high separation for the SA model, with only one region for the SA-RC model. Larger differences are also seen in the root region, where the onset of separation is seen for the the simulation using the SA-RC simulation. The skin friction is also significantly reduced for the SA-RC simulation when compared to the SA simulation in the region where the chine and outer inboard flap

17

(a) SA, $\alpha = 11.29^o$

(b) SA-RC, $\alpha = 11.29^o$

(c) SA, $\alpha = 17.05^o$

(d) SA-RC, $\alpha = 17.05^o$

(e) SA, $\alpha = 19.57^o$

(f) SA-RC, $\alpha = 19.57^o$

(g) SA, $\alpha = 21.47^o$

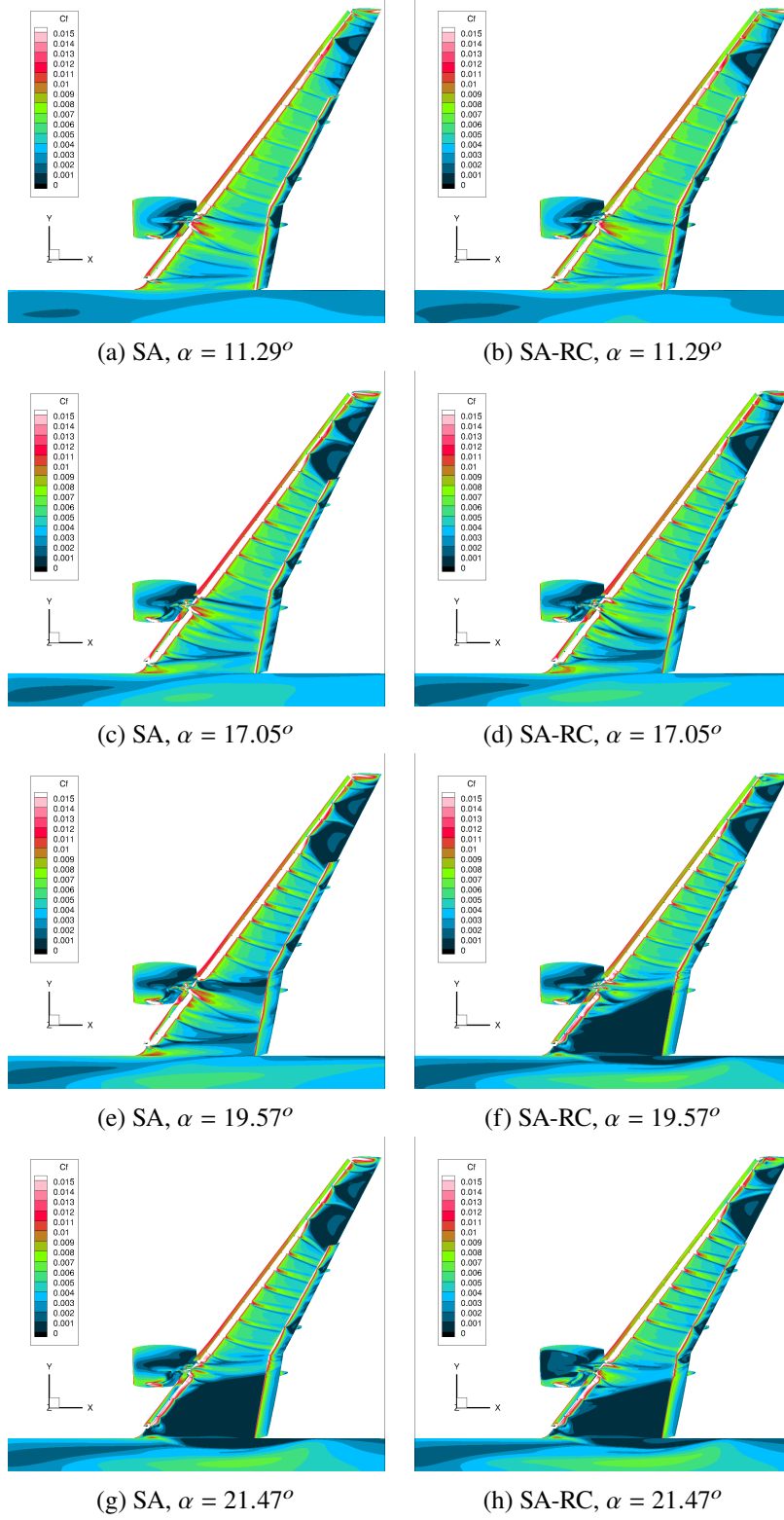(h) SA-RC, $\alpha = 21.47^o$

**Fig. 21    Comparison of the Skin friction distributions at four angles of attack for cases with the SA and SA-RC turbulence models using warm-started solutions.**

vortices pass. As the alpha is increased to $\alpha = 19.57^o$, strong root separation is seen for the SA-RC model which contributes to the drop in lift and sharp early pitching moment break. A low level of separation is seen for the SA model behind the nacelle. In the tip region, a second pocket of high separation appears for the SA-RC model, with the two models still showing high separation behind different slat brackets. Similar features were seen at $\alpha = 20.55^o$, hence not shown in this paper. At the highest angle of attack, both models predict significant separation in the root region, with the SA model showing a larger separation region that propagates further outboard near the leading edge of the wing. One interesting feature is the fully separated upper surface of the nacelle for the SA-RC model, which is not seen in the SA simulation. To examine these differences further, the vorticity and turbulent eddy viscosity ratio contours are extracted across three axial planes at two angles of attack of $11.29^o$ and $19.57^o$, shown in Figures 22-25.



| (a) SA, Cut 2 | (b) SA, Cut 3 | (c) SA, Cut 5 |

| (d) SA-RC, Cut 2 | (e) SA-RC, Cut 3 | (f) SA-RC, Cut 5 |
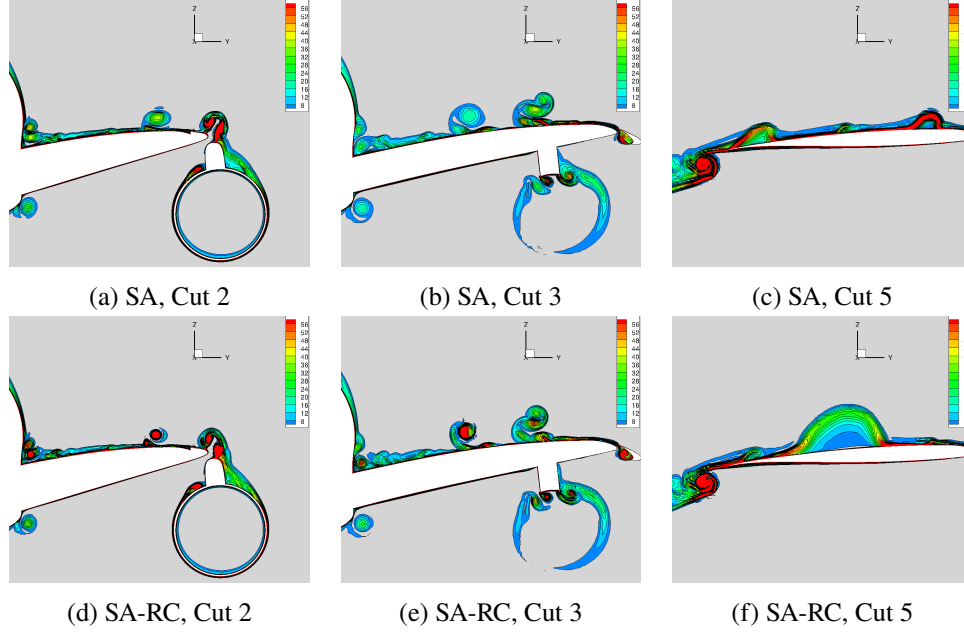
**Fig. 22   Vorticity fields at three streamwise stations and $\alpha = 11.29^o$ for SA and SA-RC turbulence models using warm-started solutions.**

At Cut 2 at $11.29^o$ the individual vortices have significantly higher peak vorticity in the vortex cores for the SA-RC model when compared to the SA model (wing-flap junction, inner inboard slat and chine vortices). At Cut 3, similar observations can be made for the flow structures above the wing. The structures below the wing in the wake of the nacelle, shows good correlation between the two turbulence models. Across the blade tip, the SA-RC model shows strong separation behind one of the slat brackets, whereas significantly weaker separation is seen for the SA model behind two slat brackets. The primarily reason behind stronger resolution of the high lift system vortices can be seen in Figure 24, where lower levels of eddy viscosity can be seen in the vortex cores. This can especially be seen at Cut 2 for the chine vortex. At Cut 3, the levels of eddy viscosity are similar for both simulations, apart from the chine vortex and the structures below the wing in the nacelle wake. At Cut 5, the regions of high eddy viscosity across the blade tip, follow the regions of high separation behind the slat brackets. At the higher angle of attack of $19.57^o$, greater differences are seen in the vorticity and eddy viscosity ratio contours, due to strong separation present in the root region for the SA-RC simulation. The chine vortex is significantly better resolved in the SA-RC simulation, with a reduced core radius and higher core vorticity. Downstream, the chine vortex dissipates quickly for the SA simulation, and remains well resolved when using the SA-RC model. At the most downstream section, Cut 5, significant separation is seen for both models, with slightly lower separation for the SA-RC model. The outer outboard flap vortices also have different formation physics. The eddy viscosity contours once again show a significant reduction in eddy viscosity in the chine vortex for the SA-RC simulations, however, the large inboard separation causes significant growth in the eddy viscosity at the root. This causes greater regions of high eddy viscosity for the SA-RC simulation at Cut 3. At Cut 5 the regions of high eddy viscosity follow the regions of high separation.

Based on the comparison of SA and SA-RC turbulence models, the SA tends to perform better for this configuration. The addition of the RC correction, clearly reduced the eddy viscosity in the vortices present in the high-lift system,
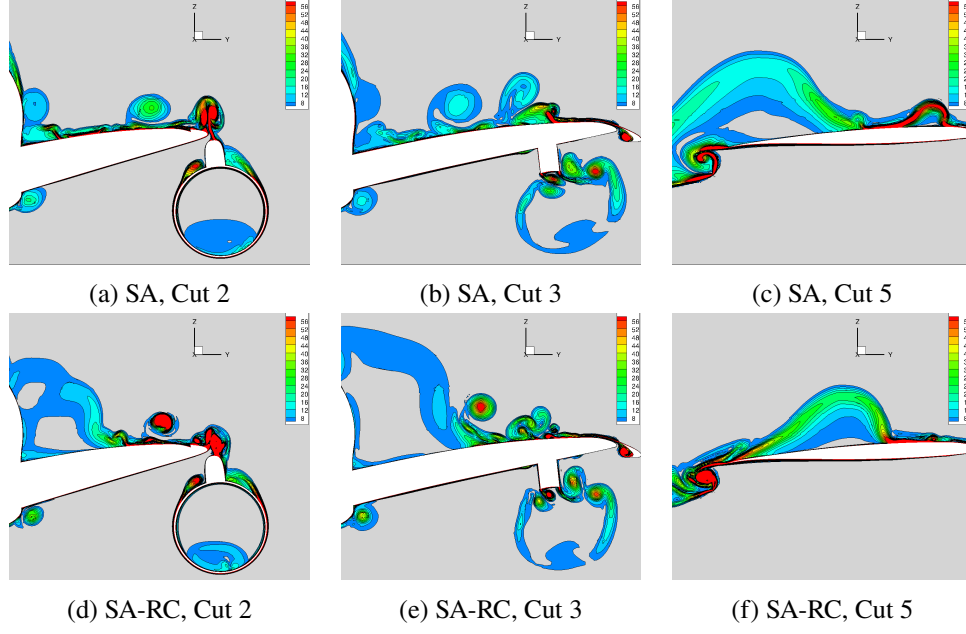
**Fig. 23   Vorticity fields at three streamwise stations and $\alpha = 19.57^o$ for SA and SA-RC turbulence models using warm-started solutions.**



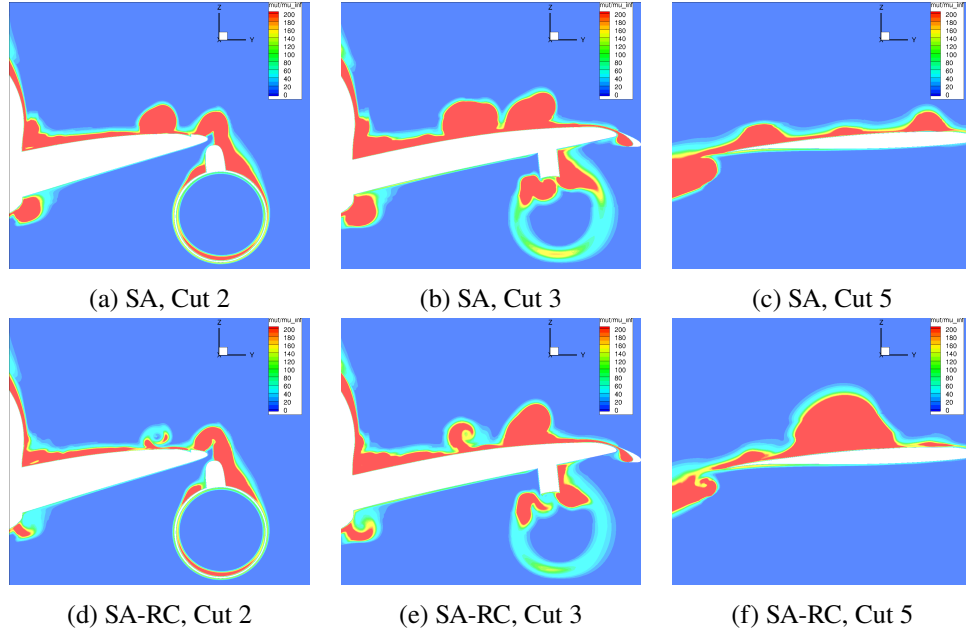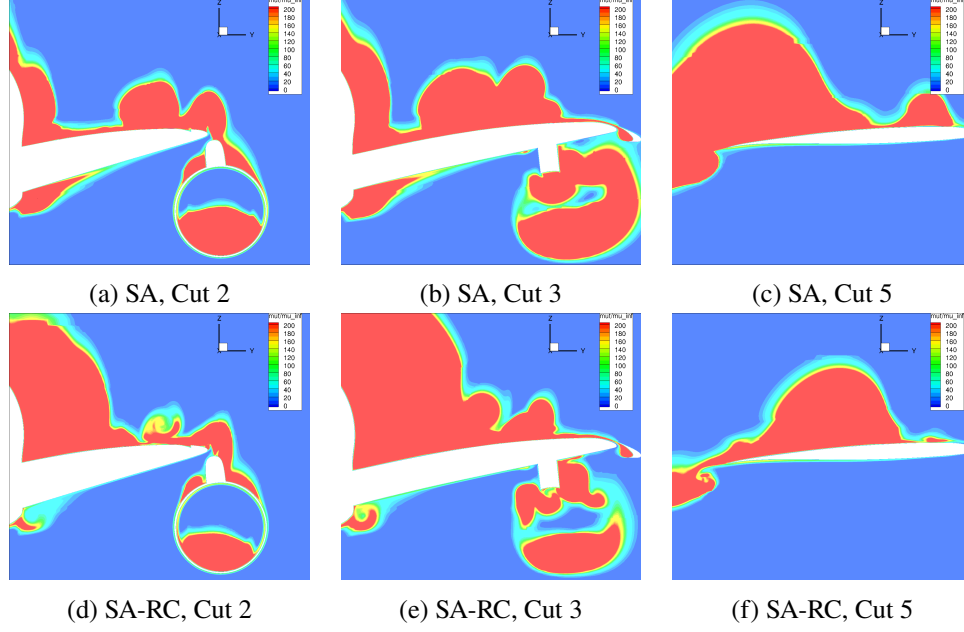**Fig. 24   Turbulent eddy viscosity ratio fields at three streamwise stations and $\alpha = 11.29^o$ for SA and SA-RC turbulence models using warm-started solutions.**

leading to higher levels of vorticity in the vortex cores. However, the SA-RC model also led to early stall at the root leading to poorer agreement when compared to experiments. For future studies, the SA model is recommended with further work necessary to assess other turbulence models such as the $k - \omega$ SST model.

(a) SA, Cut 2        (b) SA, Cut 3        (c) SA, Cut 5

(d) SA-RC, Cut 2     (e) SA-RC, Cut 3     (f) SA-RC, Cut 5

**Fig. 25** **Turbulent eddy viscosity ratio fields at three streamwise stations and** $\alpha = 19.57^o$ **for SA and SA-RC turbulence models using warm-started solutions.**

## C. Cold-start vs Warm-start Effects

Cold-start and warm-start effects are examined next. Cold-start solutions are performed by initializing the simulation from freestream, which means that the flow-field redevelops completely during the convergence of the simulation. Warm-started simulations are started by initializing the flow-field from the previous angle of attack. Two different warm-started runs were complete, starting from different angles of attack, $\alpha = 2.78^o$ and $\alpha = 17.05^o$. For the warm-start from $\alpha = 17.05^o$, all lower angles of attack (including $\alpha = 17.05^o$) used cold-start solutions, and the warm-start was started for the next $\alpha$. This cold/warm start sensitivity was seen to have an effect for other participants of the workshops as well as previous high-lift prediction workshops. The simulations in the present study were performed using the SA turbulence model and the ANSA C grid. The integrated load results are shown in Figure 26.



(a) $C_L$ vs $\alpha$        (b) $C_D$ vs $C_L$        (c) $C_M$ vs $C_L$
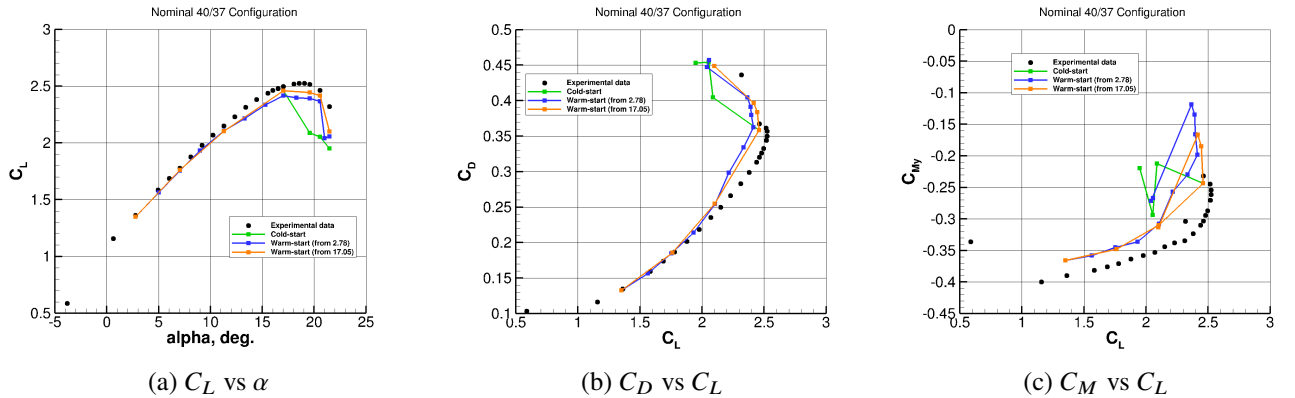
**Fig. 26** **Comparison of integrated loads for cases using cold and warm started solutions.**

The integrated loads indicate that the starting solution has a large impact on the final result. The cold-started solutions show an early stall compared to experiment with a drop in lift coefficient, increase in drag and early pitching moment break. Warm-starting the solution leads to much closer agreement with experimental data. Across the angle of attack of $17.05^o$-$20.55^o$ the lift curve is fairly flat and then sharply drops at $\alpha = 21.47^o$ when using warm-started solutions.

The agreement in drag is very good with accurate predictions of the high-$\alpha$ pitching moment break (even though the exact magnitude is underpredicted). The warm-start from $\alpha = 17.05^o$ shows better agreement with experimental data compared to the warm start from $\alpha = 2.78^o$, as the cold-started solution at $\alpha = 17.05^o$ is closer to experiment than the warm-started run. As the angle of attack is spooled-up, similar flow features can be seen for both warm-started sweeps. To analyze these differences in greater detail, the skin friction contours are extracted at four angles of attack, shown in Figure 27. At lower angles of attack, little sensitivity was seen between the different start-up approach, hence these solutions are not analyzed further.

Firstly, the cold-start and warm-start results are compared at $\alpha = 17.05^o$, which determines the primary reason behind the higher lift of the warm-start from $17.05^o$ curve. The main difference in the two results is in the tip region. Both warm-start and cold-start solutions show high unphysical separation behind two slat brackets. However, the two separation regions are located at different slat brackets for cold and warm started solutions, with the cold-started solution showing high separation at slat brackets further outboard than the warm-started solution. The outer separation region is therefore smaller for the cold-started solution leading to increased lift when compared to the warm-started solution. As the angle of attack increases similar features appear in both warm-started solutions from $2.78^o$ and from $17.05^o$, indicating that the tip region differences at $17.05^o$ remain in the solution at higher angles of attack and are the main reason behind the integrated load differences between the two warm-started sweeps. At $\alpha = 19.57^o$, the cold-started solution exhibits a large region of separation over the nacelle as well as behind the nacelle over the wing, with a much smaller reduction in skin friction over a narrow region seen for the warm-start solutions. As the angle of attack is increased to $\alpha = 20.55^o$, the root strongly separates for the cold-started solution with the warm-started solution only showing the onset of separation at the root. At the highest angle of attack of $21.47^o$ both cold-start and warm-start solutions stall at the root, with a significant region of separation over the wing past the nacelle seen for the cold-start simulation. It must also be noted that, over the range of $\alpha = 19.57^o$ to $\alpha = 21.47^o$, only minor differences are seen between the cold and warm started solutions across the blade tip region, indicating that the integration of the nacelle, pylon, chine vortices and prediction of the root separation is the main cause behind the differences seen in the integrated loads. In particular, strong separation is seen on the nacelle for the cold-started solution which is not present in the warm-started solutions. This separation will affect the flow ahead of the wing and the levels of upwash as the flow passes over the pylon, leading to different effective angles of attack seen by the wing. The flow fields are examined further by analyzing the vorticity contours at two angles of attack and four radial stations shown in Figures 28-30.

At Cut 1, the vorticity contours show close to no changes at $\alpha = 17.05^o$. At the higher angle of attack, the root region shows similar flow features, however, differences are seen over the nacelle. The cold-start solution shows high separation over the nacelle, but also a tighter chine vortex with higher peak vorticity. The nacelle separation is likely to have an effect on the chine vortex strength. Further downstream at Cut 2, the vorticity contours at $\alpha = 17.05^o$ also do not indicate any significant differences. At the higher angle of attack of $19.57^o$, strong separation past the nacelle for the cold-started solution leading to the suppression of the outer inboard flap and nacelle pylon vortex pair interaction. The other flow features, show high similarities in the root region as well as under the wing. Across the blade tip the primary effect is the different separation patterns at $\alpha = 17.05^o$ for cold-started and warm-started solutions. At higher angles of attack, the cold-started and warm-started solutions from $\alpha = 2.78^o$ show very little differences in the blade tip region.

The analysis of warm and cold-started solutions show that initializing the solution from the previous angle of attack can be favorable in RANS predictions for highly separated flows. The cold-started solutions can often develop unphysical separation during the convergence history, which will remain in the solution until the simulation is stopped. The primary differences are seen in the root region, with the prediction of nacelle separation and flow patterns over the wing past the nacelle. Certain minor differences are also seen in the tip region, with the flow exhibiting high unphysical separation past different slat brackets.

## D. Hysteresis effects

The effect of warm-started solutions is examined further by investigating the flow topology as the $\alpha$ is spooled-down. For no-hysteresis, the solutions during the $\alpha$ spool-up and spool-down should be exactly the same. To examine hysteresis effects, the ANSA C grid warm-started solutions from $2.78^o$ were used, and continued from the last $\alpha = 21.47^o$, back down to $\alpha = 9^0$. The integrated load results are shown in Figure 31.

The integrated load results indicate a strong hysteresis effect, as the lift solution does not recover to the spool-up result until $\alpha = 13.3^o$. In between $\alpha = 21.47^o$ and $\alpha = 13.3$, the spool-down results has a lower lift, higher drag with a increase in negative pitching moment. Even past $\alpha = 13.3^o$, the spool-down result does not exactly match the spool-up result, with increased drag and reduced pitching moment. To examine the behavior of the integrated loads, the skin
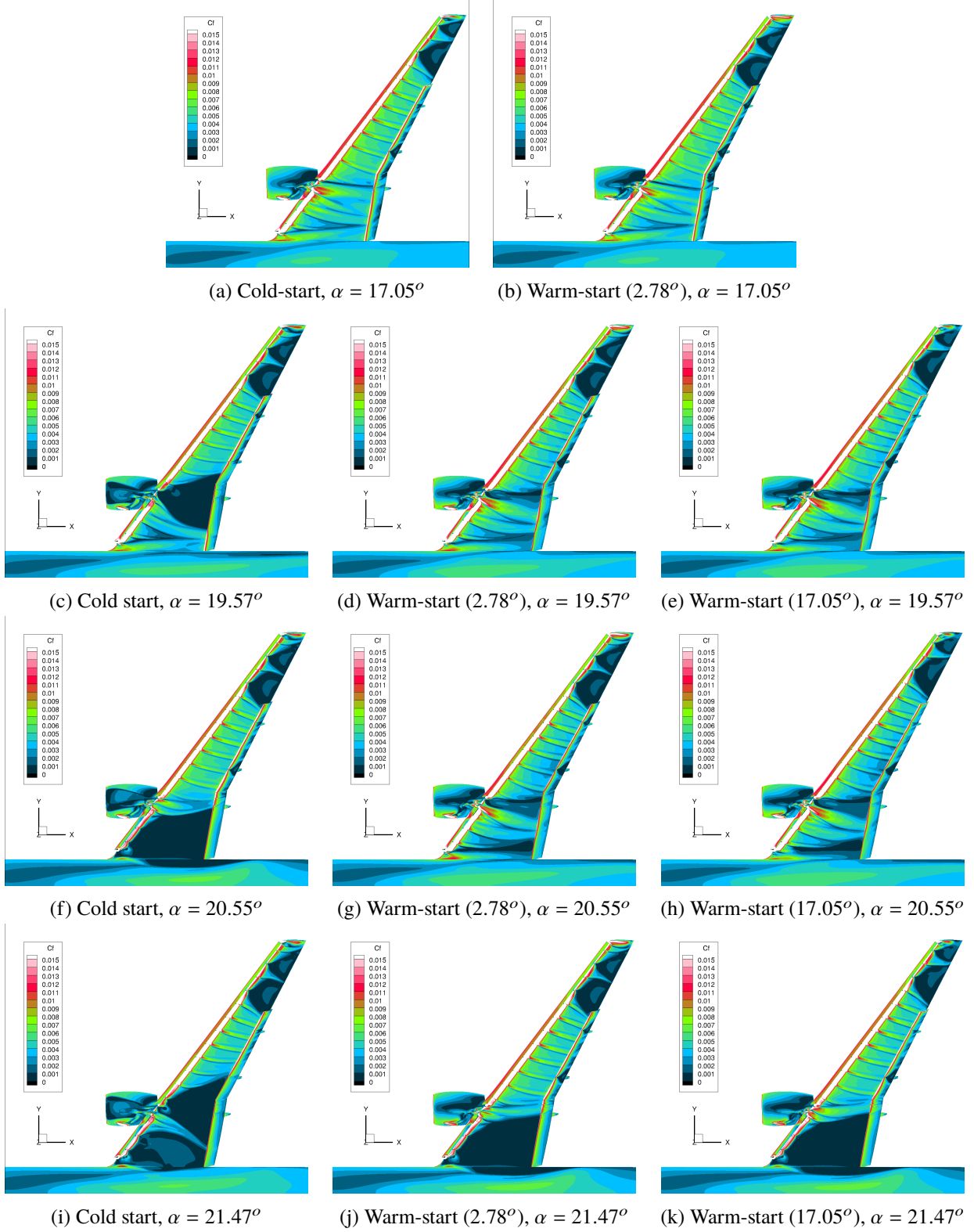
(a) Cold-start, $\alpha = 17.05^o$      (b) Warm-start $(2.78^o)$, $\alpha = 17.05^o$

(c) Cold start, $\alpha = 19.57^o$      (d) Warm-start $(2.78^o)$, $\alpha = 19.57^o$      (e) Warm-start $(17.05^o)$, $\alpha = 19.57^o$

(f) Cold start, $\alpha = 20.55^o$      (g) Warm-start $(2.78^o)$, $\alpha = 20.55^o$      (h) Warm-start $(17.05^o)$, $\alpha = 20.55^o$

(i) Cold start, $\alpha = 21.47^o$      (j) Warm-start $(2.78^o)$, $\alpha = 21.47^o$      (k) Warm-start $(17.05^o)$, $\alpha = 21.47^o$

**Fig. 27    Skin friction distributions at four angles of attack using warm-started and cold-started solutions.**

(a) Cold-start, $\alpha = 17.05^o$  (b) Warm-start ($2.78^o$), $\alpha = 17.05^o$

(c) Cold start, $\alpha = 19.57^o$  (d) Warm-start ($2.78^o$), $\alpha = 19.57^o$  (e) Warm-start ($17.05^o$), $\alpha = 19.57^o$
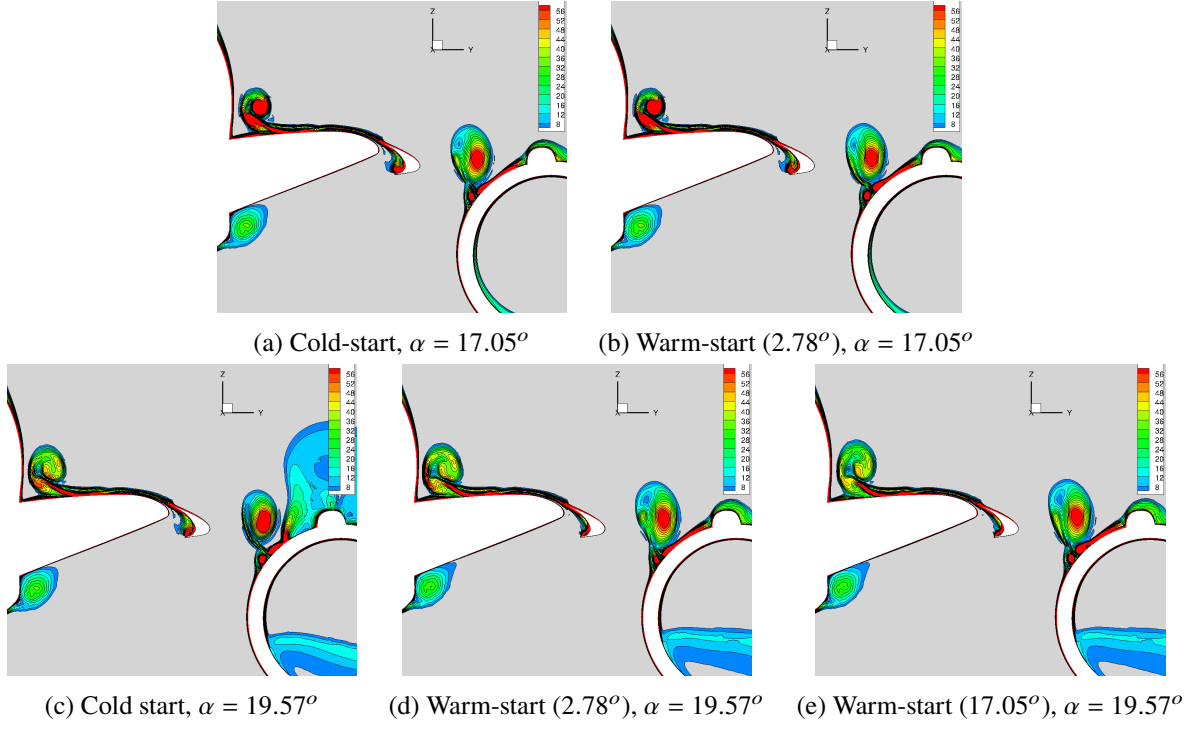
**Fig. 28  Vorticity fields over the wing in the inboard regions at Cut 1 using warm-started and cold-started solutions.**



(a) Cold-start, $\alpha = 17.05^o$  (b) Warm-start ($2.78^o$), $\alpha = 17.05^o$

(c) Cold start, $\alpha = 19.57^o$  (d) Warm-start ($2.78^o$), $\alpha = 19.57^o$  (e) Warm-start ($17.05^o$), $\alpha = 19.57^o$
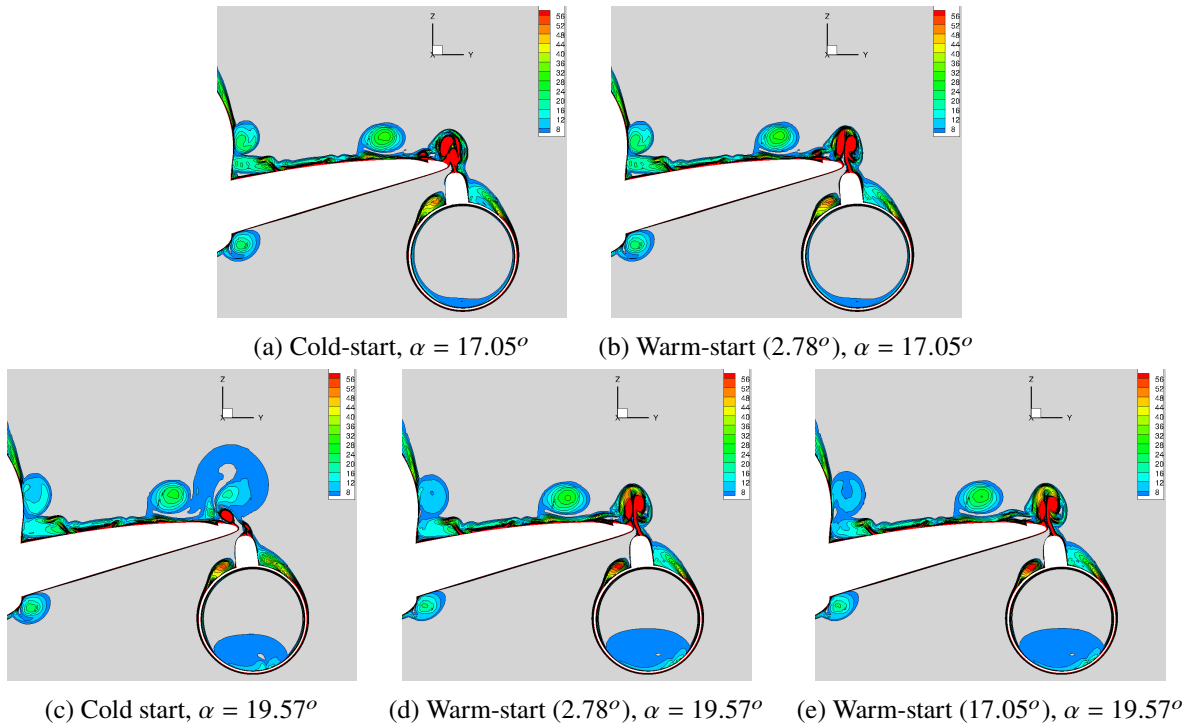
**Fig. 29  Vorticity fields over the wing in the inboard regions at Cut 2 using warm-started and cold-started solutions.**

24

(a) Cold-start, $\alpha = 17.05^o$     (b) Warm-start (2.78$^o$), $\alpha = 17.05^o$

(c) Cold start, $\alpha = 19.57^o$    (d) Warm-start (2.78$^o$), $\alpha = 19.57^o$    (e) Warm-start (17.05$^o$), $\alpha = 19.57^o$
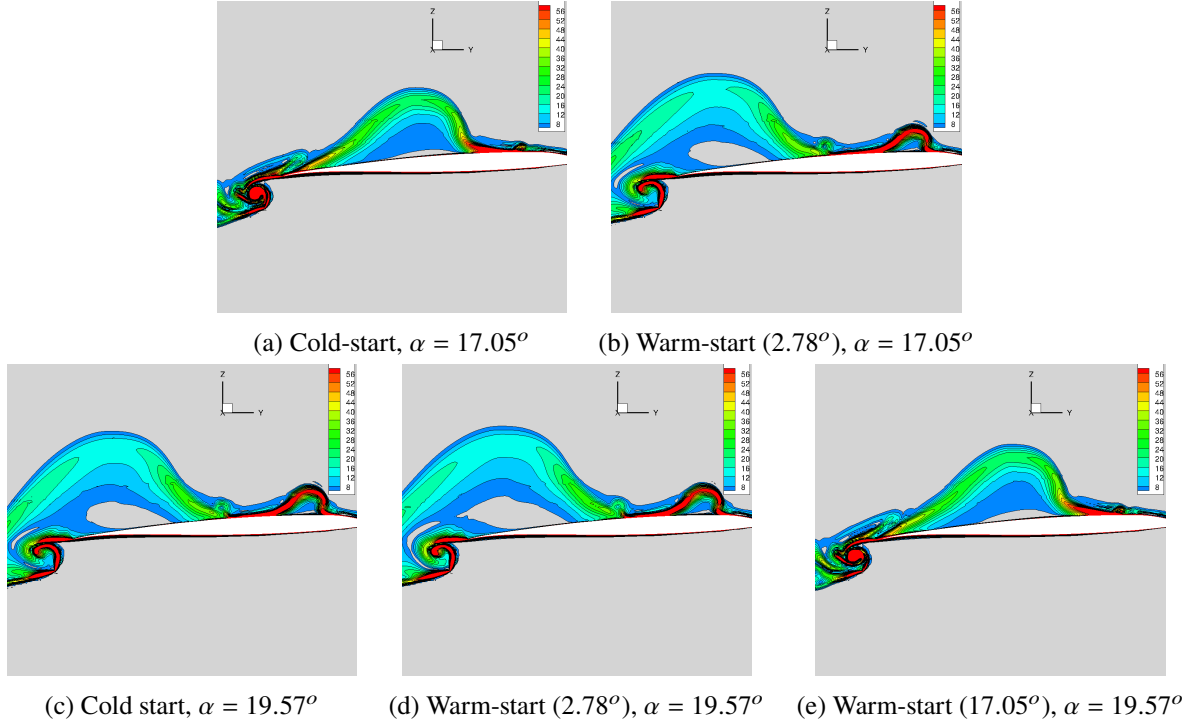
**Fig. 30** **Vorticity fields over the wing in the inboard regions at Cut 5 using warm-started and cold-started solutions.**



(a) $C_L$ vs $\alpha$      (b) $C_D$ vs $C_L$      (c) $C_M$ vs $C_L$
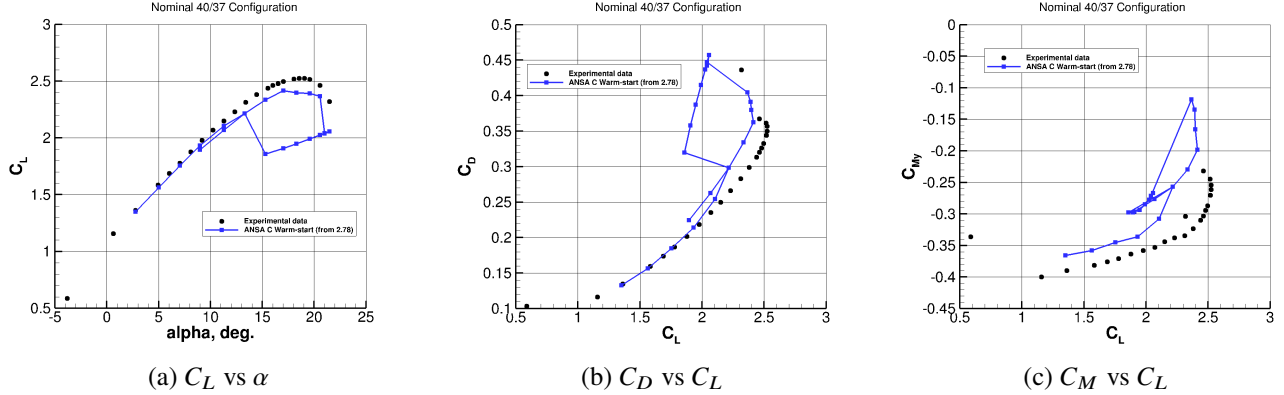
**Fig. 31** **Integrated loads for the hysteresis case study based on the ANSA C grid.**

friction distributions are shown in Figure 32 at three angle of attack.

The skin friction distributions, show significant differences between the spool-up and spool-down results. At $\alpha = 20.55^o$ and $\alpha = 17.05^o$ the spool-down results exhibit significant separation regions at the root, which was present in the $\alpha = 21.47^o$ result. The separation does not reattach until the $\alpha$ is spooled-down to 13.3$^o$. The spool-up and spool-down results show similar features across the blade tip and nacelle at $\alpha = 20.55^o$ and $\alpha = 17.05$. As the $\alpha$ is spooled-down further to 11.29$^o$, the skin friction patterns in the root region show high similarities. The main difference between the spool-up and spool-down results is in the tip region, where the high separation behind the slat brackets does not reduce for the inboard slat bracket wake. This is the main reason behind the reduced pitching moment and increased drag for the spooled-down result.

The hysteresis results are not analyzed further, as the validity of the findings is questioned. The overall integrated loads prediction at 21.47$^o$ based on a RANS simulation is quite poor when compared to experiments, with a high

(a) $\alpha = 11.29^o$, Spool-up     (b) $\alpha = 17.05^o$, Spool-up     (c) $\alpha = 20.55^o$, Spool-up

(d) $\alpha = 11.29^o$, Spool-down     (e) $\alpha = 17.05^o$, Spool-down     (f) $\alpha = 20.55^o$, Spool-down
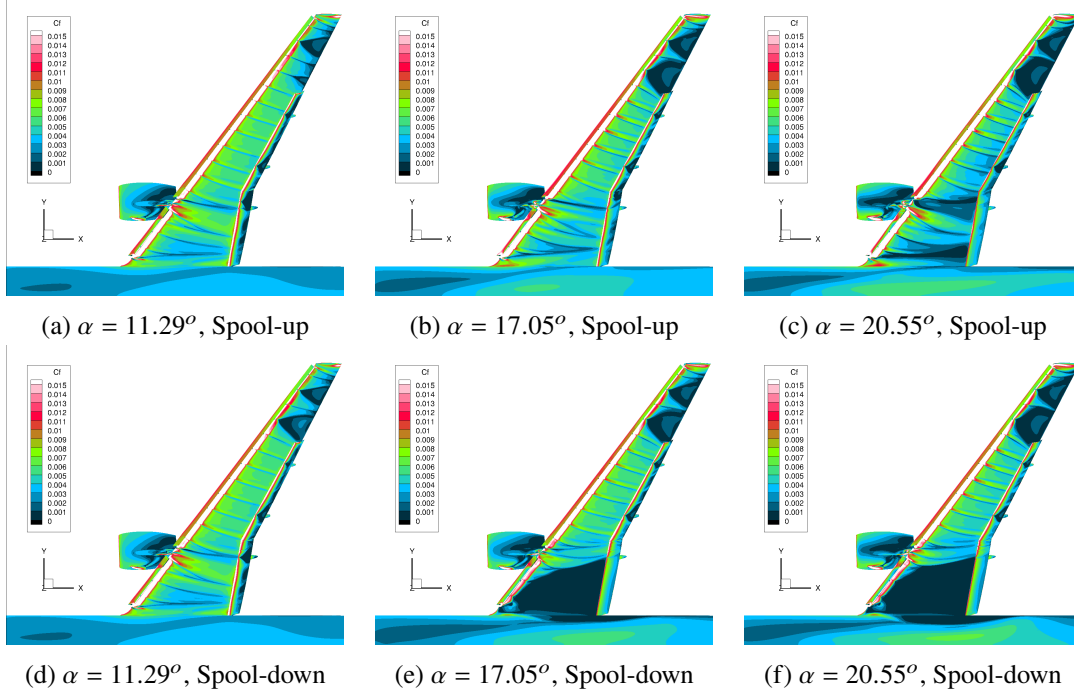
**Fig. 32**    **Skin friction distributions at three angles of attack during $\alpha$ spool-up and spool-down.**

underprediction in lift and overprediction in drag, which likely leads to overpredicted separation regions near the root as well as across the wing tip. The physical hysteresis effects are expected to be much lower than seen in the present results with a much lower separation inboard. Furthermore, further work is required in the use of steady RANS versus unsteady RANS or DDES approaches in the study of hysteresis effects.

### E. Analysis of Best Practice Results

The ANSA C warm-started simulations with the SA turbulence model are considered as the best practice results. Further analysis of these results is performed by comparing with available experimental data as well as DDES simulations near $C_{L_{MAX}}$ to further assess the suitability of steady RANS for high-lift predictions. The DDES simulations are performed at $\alpha = 19.57^o$ and $21.47^o$ using cold-started solutions on the ANSA C grid with no modifications. A time step of $4 \times 10^{-4} s$ corresponding to a non-dimensional time-step of $3.88 \times 10^{-3}$, which is defined using the convective time unit (CTU) definition: $\Delta t u_{ref}/C_{MAC}$. The DDES simulations were performed for 40 CTU's for $\alpha = 19.57^o$ and 80 CTU's for $\alpha = 21.47^o$, with the last 20 CTU's used for solution averaging for $\alpha = 19.57^o$ and 40 CTU's used for $\alpha = 21.47^o$. The integrated load results are shown in Figure 33, with the error bars for the DDES simulations corresponding to splitting the signal into 10 samples (2 CTU's for $\alpha = 19.57^o$, 4 CTU's for $\alpha = 21.47^o$) and computing the standard error of the sample means based on a 95% confidence interval.

Based on figure 33, significant improvements for high-lift predictions can be obtained by moving to DES simulations. At $19.57^o$, the drag and moment predictions are excellent with very good agreement in the lift coefficient, whereas at $21.47^o$ excellent agreement is obtained for all three coefficients. To examine the integrated loads results in further detail and to determine whether any error cancellation effects exist, the surfaces pressures are extracted from the solutions and compared with best-practice RANS results and experimental data shown in Figures 34-36 at three angles of attack ($\alpha = 7.05^o$ showing only RANS). The location of the spanwise slices can be seen in Figure 2.

The surface pressure predictions at $\alpha = 7.05^o$ show good agreement for RANS-based predictions with experimental data. The RANS-based solutions are able to accurately predict the pressure coefficient the root regions and mid-span portions of the wing. Some minor differences exist at cut C, due to the interaction with the nacelle. The suction regions over the slat, wing and flap are also slightly underpredicted in the wing tip region. At $\alpha = 19.57^o$, for the most inboard cut A, RANS actually performs slightly better than DES. The DES simulation is highly unsteady in this region and leads to an underprediction of the suction peak over the wing. Certain uncertainties exist at this location, as the impact of

(a) $C_L$ vs $\alpha$  (b) $C_D$ vs $C_L$  (c) $C_M$ vs $C_L$
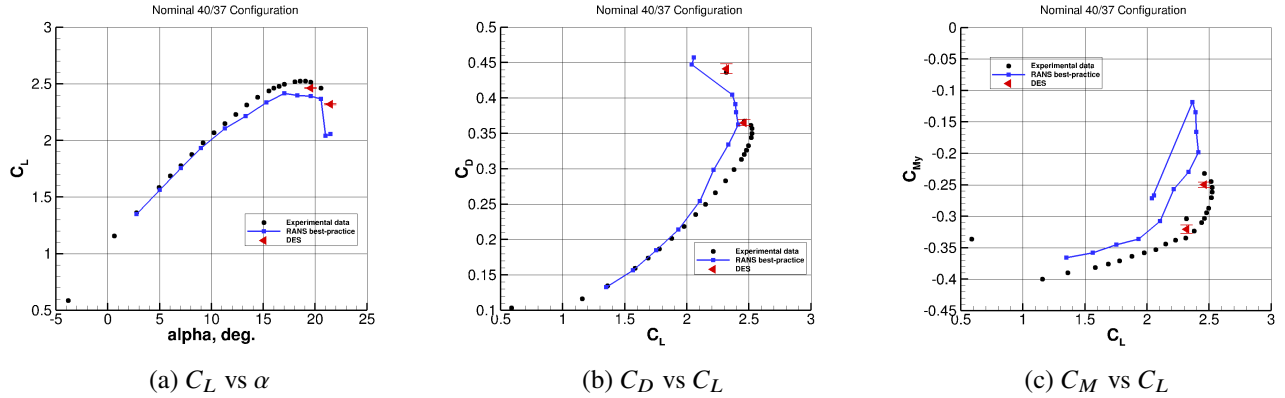
**Fig. 33  Comparison of integrated loads for best-practice RANS and DES simulations.**

including the test stand in the simulation will have the largest impact at this axial station. Further outboard at cut B, both RANS and DES simulation lead to good agreement with experimental data, with a again a slightly lower suction peak at the wing leading edge predicted by the DES simulation. At cut C, the DES show significant improvement over RANS, with improved predictions of the wing suction peak, as well as pressure towards the trailing edge region and distribution over the flap. At cuts D and E, the predictions are between RANS and DES are fairly similar with both approaches leading to good predictions when compared to experimental data. At these cuts, however, the complexity of the flow physics are reduced, as the flow remains attached of the mid-portion of the wing. The main benefit of DES is seen in the blade tip region at cuts G and H, where RANS predicts sharp separation past the slat brackets. The DES pressure curves indicate attached flow and show excellent agreement with experimental data. At the highest angle of attack of $21.47^o$ the greatest benefits of DES are obtained. In the inboard cuts, the slat and wing suction peaks are underpredicted, but the DES predictions show excellent agreement on the wing in the adverse pressure gradient prediction when compared to experimental data. This is a significant improvement over RANS, which indicates are very strong separated flow in these locations. At locations C through F, the DES simulations follow the experimental pressure curves very accurately yielding minor benefits over RANS at the station. At the most outboard stations G and H, once again the DES simulation leads to excellent agreement with experimental data, which RANS fails to capture. The solutions are analyzed in greater detail by extracting the skin friction contours shown in Figure 37 at $\alpha = 19.57^o$ and $\alpha = 21.47^o$.

The skin friction distributions show the viability of DES for high-lift predictions over the RANS-based approach. At both examined angles of attack the DES simulations capture the slat bracket wakes more accurately with significantly reduced separated flow regions of the wing tip. This is the greatest benefit of DES, and the primary reason behind improved integrated load predictions. Further inboard, the DES simulation does not predict any drop in skin friction in the flow past the nacelle. The root region also appears to show lead to large differences between the steady RANS and DES predictions. The DES simulation at $\alpha = 19.57^o$, shows a minor recirculation region at the root coming from trailing edge, which is not present in the RANS solution. The prediction at $\alpha = 21.47^o$ for the DES simulation is significantly improved with reduced separation present over the root region of the wing compared to the RANS solution. A strong drop in skin friction can, however, be seen at the wing horn. To analyze the surface flow in greater detail, surface streamlines are extracted from the solution and compared with experimental oil flow patterns shown in Figures 38-39.

Upon examination of the surface streamlines it can be stated, that many of the flow features seen in the DES simulations can be considered as plausible. At $\alpha = 19.57^o$ in the root region, the shape of the main dividing streamlines are similar to the oil flow picture with similar flow patterns around the wing horn. The main aspect of the DES solution which still holds some uncertainty is the shape of the streamlines near the trailing edge, forming a small region of recirculation. The RANS streamlines show reduced spanwise flow when compared to the DES and experimental results, with the streamlines at the root oriented towards the downstream direction and traveling less inboard. The separation patterns on the nacelle also appear to be more realistic for the DES simulation. At $\alpha = 21.47^o$, the entire root is separated for the RANS solution, leading to limited resemblance with experimental data. The DES simulation shows a higher degree of similarity with the experimental oil flow, with a similar root flow topology. Over the wing tip, the DES simulations lead to very good agreement with experimental data at both angles of attack, significantly reducing the
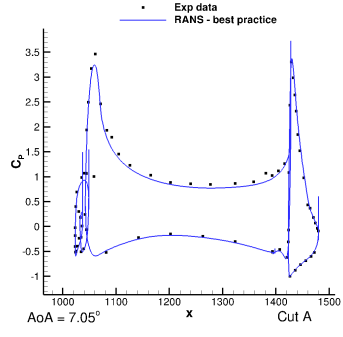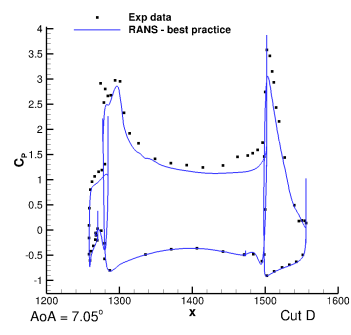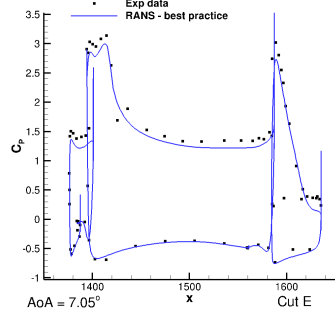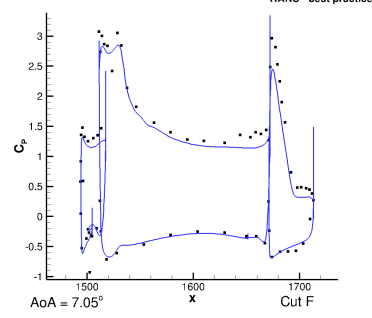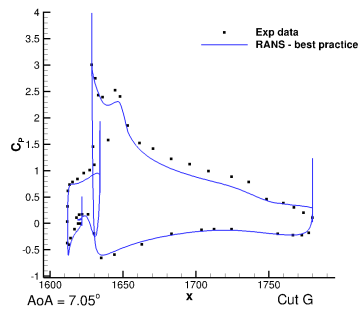
(a) Cut A
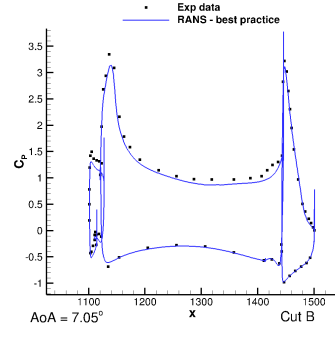
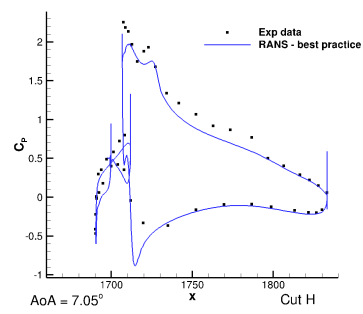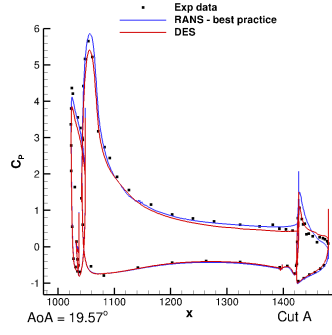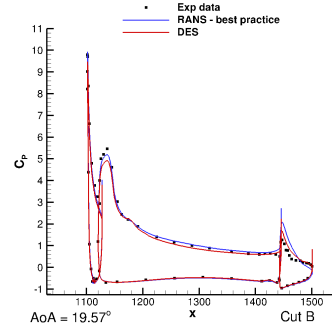(b) Cut B
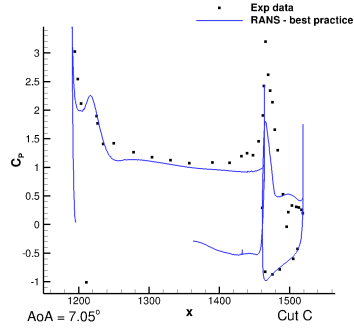
(a) Cut C

(b) Cut D

(a) Cut E

(b) Cut F

(a) Cut G
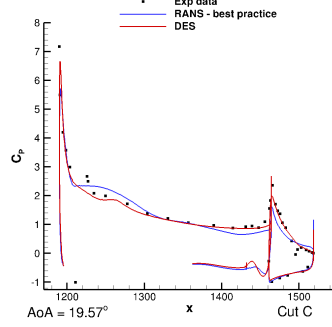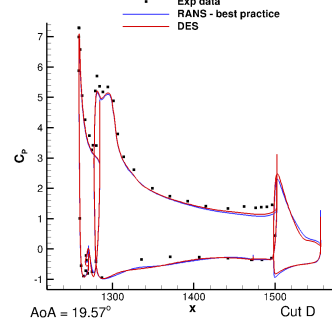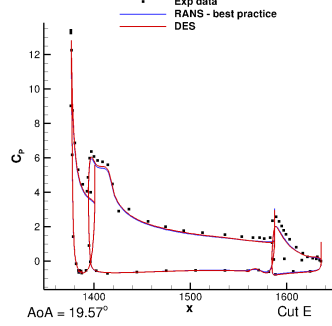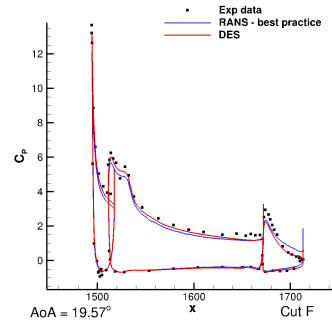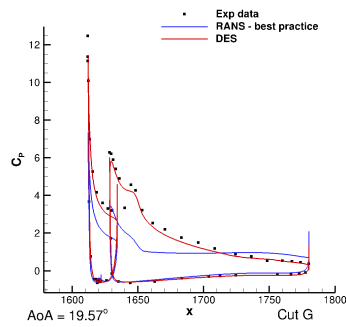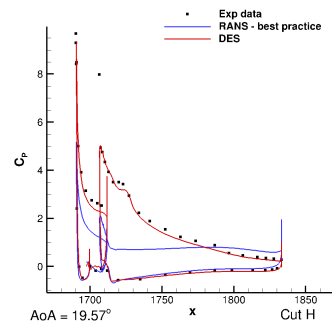
(b) Cut H

**Fig. 34    Comparisons of RANS best-practice results with experimental data at** $\alpha = 7.05^o$**.**

28

(a) Cut A            (b) Cut B

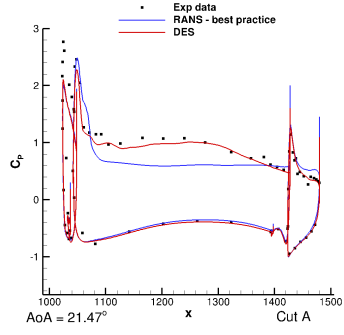(a) Cut C            (b) Cut D
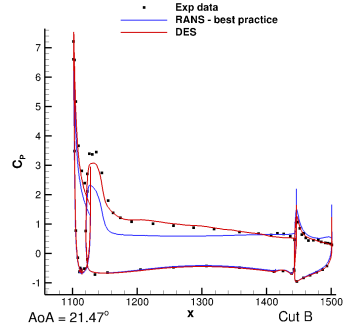
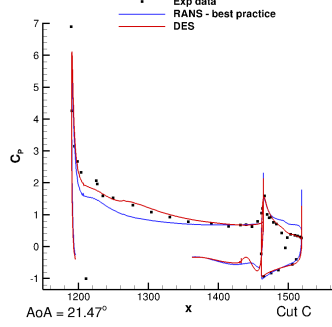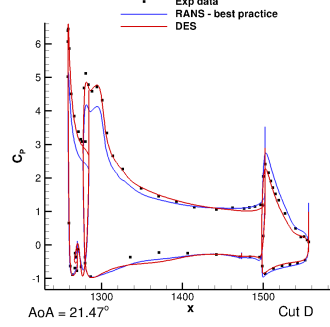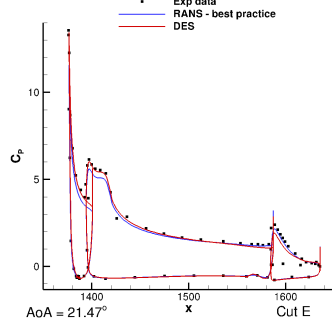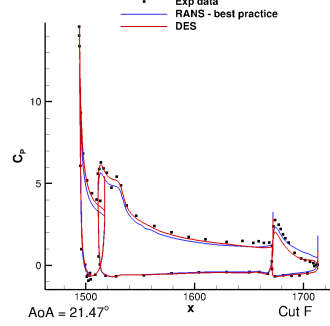(a) Cut E            (b) Cut F

(a) Cut G            (b) Cut H

**Fig. 35 Comparisons of RANS best-practice results with DES predictions and experimental data at $\alpha = 19.57^o$.**

(a) Cut A          (b) Cut B

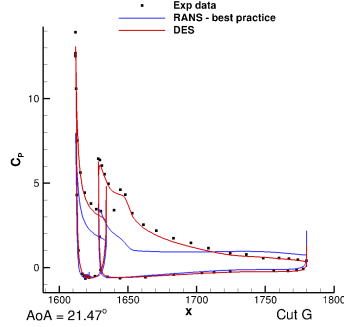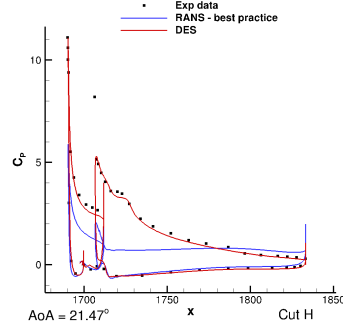(a) Cut C          (b) Cut D

(a) Cut E          (b) Cut F

(a) Cut G          (b) Cut H

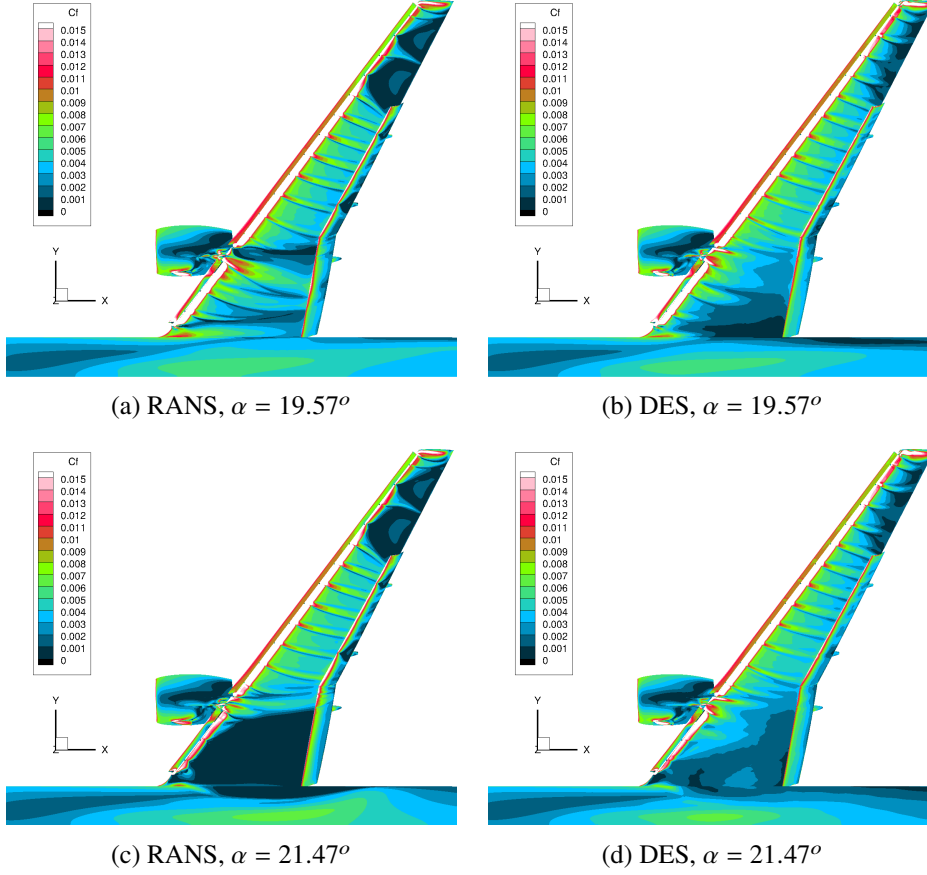**Fig. 36    Comparisons of RANS best-practice results with experimental data at $\alpha = 21.47^o$.**

(a) RANS, $\alpha = 19.57^o$  (b) DES, $\alpha = 19.57^o$

(c) RANS, $\alpha = 21.47^o$  (d) DES, $\alpha = 21.47^o$

**Fig. 37  Comparison of skin friction distributions for RANS and DES simulations at two angles of attack of** $\alpha = 19.57^o$ **and** $\alpha = 21.47^o$**.**

levels of separation when compared to RANS.

For additional analysis of the DES results the instantanous skin friction and Q-criterion flow fields are shown in Figures 40-41. The instantaneous skin friction contours and isosurface of Q-criterion indicate the the flow is highly unsteady over the wing in the root regions inboard of the nacelle. This is due to unsteady interactions between multiple vortices. A certain level of unsteadiness is also present in the tip region over the wing due to the slat brackets wakes, which were poorly captured when using the RANS-based approach.

## V. Conclusions

The current paper analyzed the various modelling sensitivities for RANS-based solutions and provided a number of recommendations including:

- RANS-based approaches show a high grid sensitivity and therefore require intelligent grid design aimed at resolving all the complex interactions present in the flow field, whether through user iteration on the mesh resolution or through mesh adaptation.
- The current results indicate the existence of multiple solutions when using RANS, with the best-practice results obtained when initializing the flow field from the previous angle of attack.
- The SA turbulence model is recommended for high-lift predictions and showed better behavior near stall than the SA-RC model.

Despite recommendations for best RANS practices, however, the further analysis of the RANS results along with DES simulations highlighted the shortcomings of RANS-based solutions and the need for scale-resolving simulations for accurate high-lift predictions. The DES results were obtained for the first grid examined and showed high confidence in
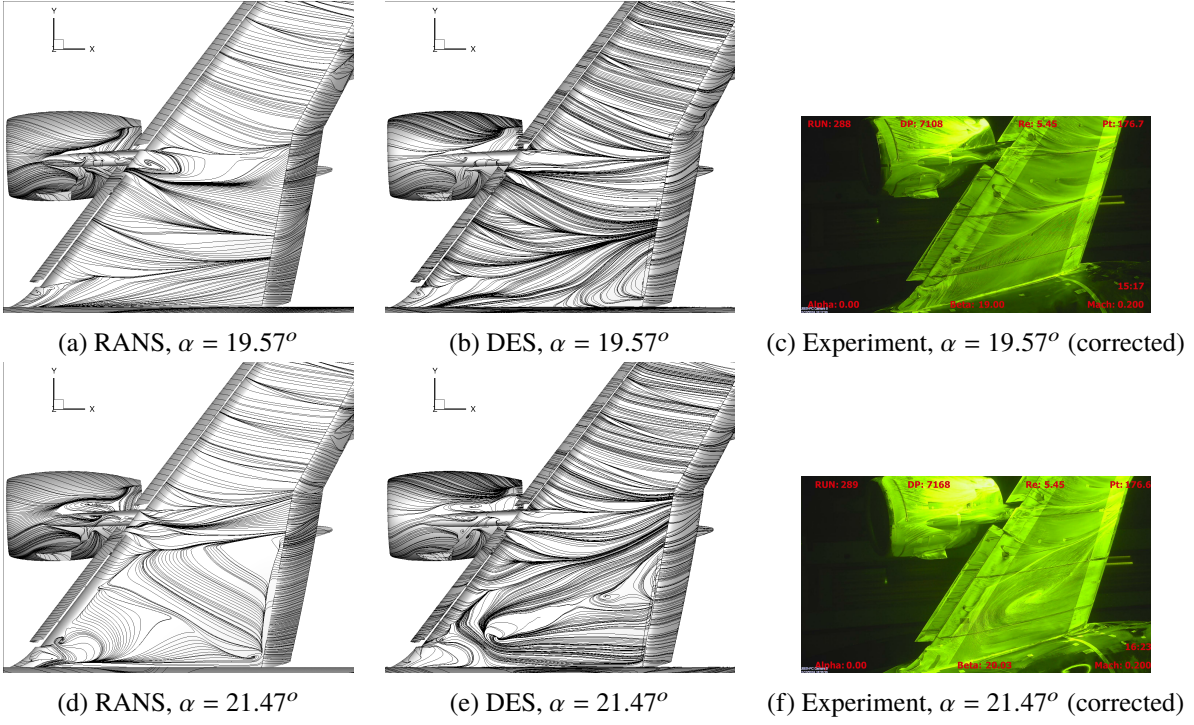
(a) RANS, $\alpha = 19.57^o$

(b) DES, $\alpha = 19.57^o$

(c) Experiment, $\alpha = 19.57^o$ (corrected)

(d) RANS, $\alpha = 21.47^o$

(e) DES, $\alpha = 21.47^o$

(f) Experiment, $\alpha = 21.47^o$ (corrected)

**Fig. 38    Comparisons of surface streamlines at two angles of attack with experimental oil flow pictures in the root region [2].**



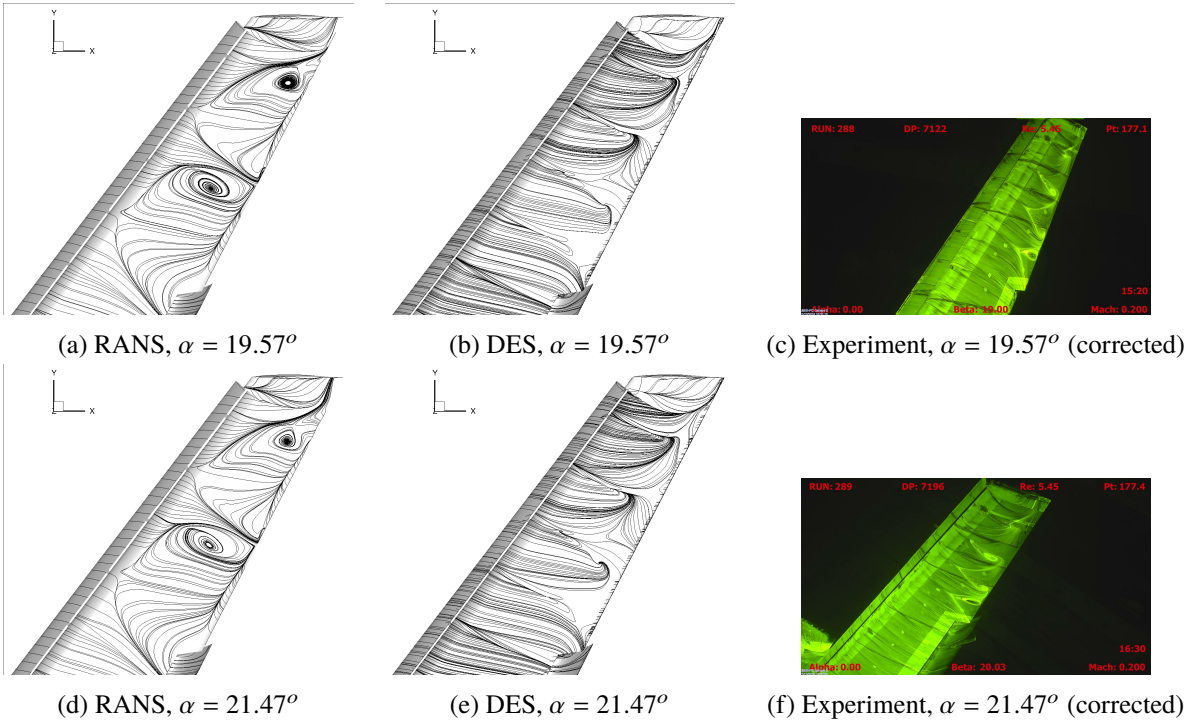(a) RANS, $\alpha = 19.57^o$

(b) DES, $\alpha = 19.57^o$

(c) Experiment, $\alpha = 19.57^o$ (corrected)

(d) RANS, $\alpha = 21.47^o$

(e) DES, $\alpha = 21.47^o$

(f) Experiment, $\alpha = 21.47^o$ (corrected)

**Fig. 39    Comparisons of surface streamlines at two angles of attack with experimental oil flow pictures in the tip region [2].**

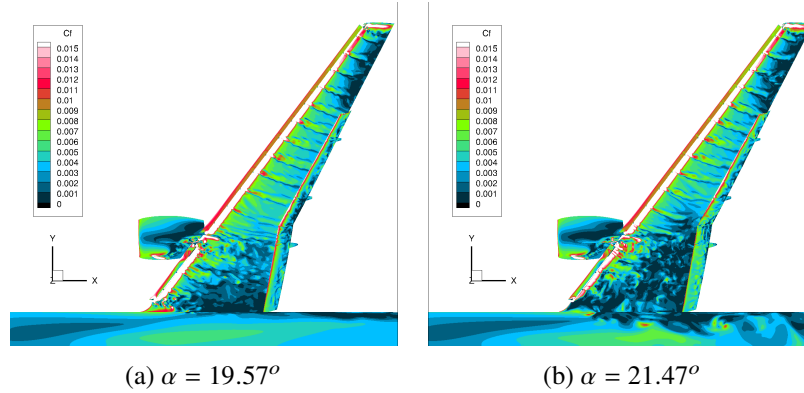(a) $\alpha = 19.57^o$          (b) $\alpha = 21.47^o$

**Fig. 40     Instantaneous skin friction contours for the DES simulations at two angles of attack.**



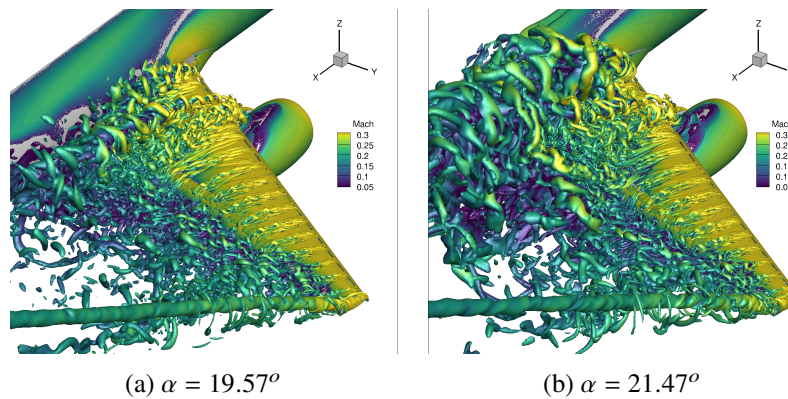(a) $\alpha = 19.57^o$          (b) $\alpha = 21.47^o$

**Fig. 41     Instantaneous isosurfaces of Q-criterion (value of 1e-7) colored with Mach number for the DES simulations at two angles of attack.**

terms of achieving the correct answer for the correct reasons. While further tweaking of turbulence models and reducing RANS grid sensitivity with sensible grid design or mesh adaptation can still keep RANS in the loop, at a certain point, the model is simply not suitable for the flow physics, as seen in the behavior of RANS in capturing the slat bracket wakes. The DES simulations are able to capture the flow physics of high-lift flows with a large degree of accuracy, although lead to a significant increase in computational costs. However, with constantly growing computational power and need for more accurate CFD predictions, scale-resolving simulations are likely to be more prominent in future high-lift prediction workshops.

## References

[1] J. Slotnick, "CFD Prediction for High Lift Aerodynamics - Recent Progress and Emerging Opportunities," RAeS Conference on Aerodynamics Tools and Methods in Aircraft Design, October 2019. URL https://www.aerosociety.com/media/12473/15-jeffrey-slotnick.pdf.

[2] C. Rumsey, "4th AIAA High Lift Prediction Workshop," , May 2022. URL https://hiliftpw.larc.nasa.gov/, nASA Langley Research Center.

[3] Rumsey, C., Long, M., Stuever, R., and Wayman, T., *Summary of the First AIAA CFD High Lift Prediction Workshop*, 49th AIAA Aerospace Sciences Meeting including the New Horizons Forum and Aerospace Exposition, 2011. https://doi.org/10.2514/6.2011-939.

[4] Rumsey, C. L., and Slotnick, J. P., "Overview and Summary of the Second AIAA High-Lift Prediction Workshop," *Journal of Aircraft*, Vol. 52, No. 4, 2015, pp. 1006–1025. https://doi.org/10.2514/1.C032864.

[5] Rumsey, C. L., Slotnick, J. P., and Sclafani, A. J., "Overview and Summary of the Third AIAA High Lift Prediction Workshop," *Journal of Aircraft*, Vol. 56, No. 2, 2019, pp. 621–644. https://doi.org/10.2514/1.C034940.

[6] Lacy, D. S., and Clark, A. M., *Definition of Initial Landing and Takeoff Reference Configurations for the High Lift Common Research Model (CRM-HL)*, AIAA AVIATION 2020 FORUM, 2020. https://doi.org/10.2514/6.2020-2771.

[7] Evans, A. N., Lacy, D. S., Smith, I., and Rivers, M. B., *Test Summary of the NASA High-Lift Common Research Model Half-Span at QinetiQ 5-Metre Pressurized Low-Speed Wind Tunnel*, AIAA AVIATION 2020 FORUM, 2020.

[8] C. Rumsey, "4th AIAA High Lift Prediction Workshop - Data Submittal Forms and Post-Processing Info," , May 2022. URL https://hiliftpw.larc.nasa.gov/Workshop4/DataForm.html, nASA Langley Research Center.

[9] C. Rumsey, "4th AIAA High Lift Prediction Workshop - Grids Download Page," , May 2022. URL https://hiliftpw.larc.nasa.gov/Workshop4/grids_downlaods.html, nASA Langley Research Center.

[10] Koklu, M., Lin, J. C., Hannon, J. A., Melton, L. P., Andino, M. Y., Paschal, K. B., and Vatsa, V. N., "Investigation of the Nacelle/Pylon Vortex System on the High-Lift Common Research Model," *AIAA Journal*, Vol. 59, No. 9, 2021, pp. 3748–3763. https://doi.org/10.2514/1.J059869.

[11] Kiris, C. C., Ghate, A. S., Duensing, J. C., Browne, O. M., Housman, J. A., Stich, G.-D., Kenway, G., Fernandes, L. S., and Machado, L. M., *High-Lift Common Research Model: RANS, HRLES, and WMLES perspectives for CLmax prediction using LAVA*, AIAA SCITECH 2022 Forum, 2022.